

## Local-time-dependent low-altitude ion spectra deduced from TWINS ENA images

J. Goldstein,<sup>1,2</sup> D. J. McComas,<sup>1,2</sup> P. Valek,<sup>1,2</sup> J. Redfern,<sup>1</sup> F. Søraas,<sup>3,4</sup> and D. Bazell<sup>5</sup>

Received 16 October 2012; revised 8 March 2013; accepted 8 March 2013; published 3 June 2013.

[1] In this paper, we analyze Two Wide-angle Imaging Neutral-atom Spectrometers (TWINS) stereo observations of energetic neutral atoms (ENAs) produced from the low altitude emission (LAE) region during the interval 1130–1146 UT on 6 April 2010. Geometrical calculations determine the geophysical locations of pixels at or near the LAE limb and the associated uncertainties. For our event, the two TWINS imagers observed a broad (8.4–9.2 h wide in magnetic local time (MLT)) region of LAEs on the opposing limb, possibly containing an ion boundary near dusk. The most intense LAEs were detected in a narrow range of magnetic latitude ( $67^{\circ}$ – $74^{\circ}$ ) and pitch angle ( $112^{\circ}$ – $116^{\circ}$ ). We implement a simplified thick-target approximation (TTA) to obtain ion spectra from TWINS LAEs and perform a validation study using a conjunction of the TWINS-observed LAE crescents with a simultaneous NOAA 17 polar-orbit pass slightly west of the TWINS LAEs. Since TTA is limited to the brightest portion of LAEs, we apply our analysis for pixels with at least 30% of the peak value. TWINS ion spectra are calculated for individual pixels spanning several hours of MLT. The spectra exhibit a pronounced local time dependence. For more westward MLT (and more equatorward latitude), there is a shift toward spectra that are more energetic and peaked. This spatial dependence is consistent with ion drift theory and previous observations. The peaked LAE-derived ion spectra of 6 April 2010 are notably different than those observed during much weaker disturbances, but are consistent with LAE observations from similar activity levels. These results demonstrate that with proper caution in interpreting the results, TWINS ENA imaging resolves MLT-dependent (and to a limited extent, latitude-dependent) low-altitude ion spectral shape information, simultaneously across a broad range of MLT. This study advances previous results that considered much coarser MLT structure in LAEs and augments previous statistical spectral analysis of in situ data.

**Citation:** Goldstein, J., D. J. McComas, P. Valek, J. Redfern, F. Søraas, and D. Bazell (2013), Local-time-dependent low-altitude ion spectra deduced from TWINS ENA images, *J. Geophys. Res. Space Physics*, 118, 2928–2950, doi:10.1002/jgra.50222.

### 1. Introduction

#### 1.1. TWINS Low Altitude Emission (LAE)

[2] Two Wide-angle Imaging Neutral-atom Spectrometers (TWINS) is a NASA mission of opportunity that performs simultaneous energetic neutral atom (ENA) imaging from two spacecraft on widely separated Molniya orbits [McComas *et al.*, 2009a]. TWINS measures ENAs over a broad energy range (1–100 keV) with high angular ( $4^{\circ} \times 4^{\circ}$ ) and time ( $\sim 1$  min) resolution.

[3] The ENA imaging of the storm time terrestrial ring current was first demonstrated by Roelof [1987], using data from the ISEE 1 spacecraft. The decades that followed saw numerous studies using ENA imaging to discern the global dynamics of space environments throughout and to the very edge of the Solar System: at Earth by the Polar, Astrid, IMAGE, and TWINS missions [Henderson *et al.*, 1997; Barabash *et al.*, 1997; Pollock *et al.*, 2001; Brandt *et al.*, 2002; Mitchell *et al.*, 2003; Brandt *et al.*, 2004; McComas *et al.*, 2009a; Bazell *et al.*, 2010; Buzulukova *et al.*, 2010; Fok *et al.*, 2010; Ilie *et al.*, 2012], at Jupiter [Mauk *et al.*, 2003], Saturn, and its moon Titan [Mitchell *et al.*, 2005a, 2005b] by the Cassini mission, and at the interstellar boundary by Cassini [Krimigis *et al.*, 2009] and IBEX [McComas *et al.*, 2009b]. Magnetospheric ENAs are created by charge exchange, in which electrons from the neutral exosphere [Zoennchen *et al.*, 2010; Bailey and Gruntman, 2011] are captured by energetic ions, rendering them neutral and thus freeing them from the geomagnetic field. ENA imaging captures these escaping neutrals and uses them to diagnose the system-level dynamics of the ring current [Valek *et al.*, 2010;

<sup>1</sup>Southwest Research Institute, San Antonio, Texas, USA.

<sup>2</sup>Department of Physics and Astronomy, University of Texas San Antonio, Texas, USA.

<sup>3</sup>University of Bergen, Bergen, Norway.

<sup>4</sup>Birkeland Centre for Space Science, Bergen, Norway.

<sup>5</sup>The Johns Hopkins University Applied Physics Laboratory, Laurel, Maryland, USA.

Corresponding author: J. Goldstein, Southwest Research Institute, San Antonio, TX, USA. (jgoldstein@swri.edu)

*Keesee et al.*, 2011, 2012; *Goldstein et al.*, 2012b; *McComas et al.*, 2012], and in many cases uses forward modeling or inversion techniques to reconstruct the global energetic ion distribution [*Roelof and Skinner*, 2000; *Perez et al.*, 2001; *Vallat et al.*, 2004; *Grimes et al.*, 2010; *Perez et al.*, 2012].

[4] The ENA imaging captures two fundamental processes of magnetospheric ions: injection and precipitation, i.e., the source and loss of the ring current. Often the brightest signal in an ENA image is the low-altitude emission (LAE), produced by ions from just outside the loss cone, mirroring in the oxygen exobase. The LAE is generated by the multiple-collision (thick-target) interaction of precipitating energetic ions with the atomic oxygen exosphere at altitudes of a few to several hundred kilometers [*Roelof and Skinner*, 2000]. Energetic ions precipitating at these altitudes typically undergo hundreds of charge exchange and stripping interactions as they spiral downward along magnetic field lines, continually changing their charge state from ion to neutral and back to ion again [*Roelof and Skinner*, 2000; *Brandt et al.*, 2001a]. A large fraction of the particles mirror and then emerge upward as ENAs that can be imaged. Energetic neutrals from LAEs were observed by the Poleward Leap sounding rocket which flew through a proton arc [*Søråas and Aarsnes*, 1996]. The first images of LAEs were produced with high-spatial resolution by the Swedish microsatellite *Astrid* [*Brandt et al.*, 2001b]. Subsequently, the IMAGE mission routinely observed LAEs in images produced by its three ENA cameras [*Pollock et al.*, 2001; *Mitchell et al.*, 2003; *Pollock et al.*, 2009]. ENA emissions originating from both the proton aurora and the main ring current have been observed at low altitudes by NOAA [*Søråas and Sørbø*, 2012]. LAEs are a ubiquitous feature of TWINS stereo images, even during extremely mild disturbances, e.g., TWINS first-light stereo images from 15 June 2008, during a corotating interaction region (CIR)-driven event [*McComas et al.*, 2009a].

[5] Multiple studies have investigated TWINS LAEs. *Valek et al.* [2010] employed the continuous coverage provided by the two TWINS spacecraft to determine the relative timing between LAE precipitation signatures and the trapped ring current emission (RCE), finding that for the storm on 22 July 2009, the global precipitating ion flux peaked earlier than the that of the trapped ions. Here the LAEs were characterized by brightest pixel inside  $2 R_E$ . In a follow-up study, *Buzulukova et al.* [2012] combined TWINS and NOAA observations from two storms and found that the relative timing between the LAE (defined as the brightest pixel inside  $1.5 R_E$ ) and RCE is controlled by the degree to which the loss cone is full or empty during the main phase of the storm. *McComas et al.* [2012] examined the timing and energy dependence of LAEs (here defined as the average ENA flux inside  $2 R_E$ ) in relation to the arrival of shock at the magnetopause, finding a sudden intensification of higher-energy LAEs roughly 15 min after the shock arrival, with an energy dispersion such that progressively lower energies appeared over the following 20 min.

[6] Unlike the optically thin emissions from the trapped ring current which involve only a single charge-exchange collision along the imaging line of sight [e.g., *Brandt et al.*, 2004], LAEs result from multiple charge exchange and stripping interactions between energetic ions and the dense, neutral oxygen exosphere, as noted above.

*Bazell et al.* [2010] analyzed TWINS LAE observations via a thick-target approximation (TTA) that accounts for the multiple exospheric collisions, to extract the shape of the precipitating ion spectrum from the ENA spectrum. For a weakly disturbed event, their derived TWINS ion spectra were found to follow (roughly) an  $(\text{Energy})^{-1}$  dependence, inconsistent with both a thermal proton spectrum and a kappa distribution for reasonable values of  $kT$  or  $\kappa$ . *Bazell et al.* defined the LAE as the multipixel-averaged ENA flux within a manually selected region of the image, and the region was correlated with appropriately scaled ion structures in simultaneous DMSP measurements.

## 1.2. Overview of LAE Case Study: 6 April 2010

[7] As mentioned above, in published works [*Bazell et al.*, 2010; *Valek et al.*, 2010; *McComas et al.*, 2012; *Buzulukova et al.*, 2012], the LAE has been characterized by either a peak value inside a fixed geocentric radius or as an average flux within a predetermined region (either inside a fixed radius or within a manually selected region). In this paper we investigate the pixel-to-pixel magnetic local time (MLT) dependence of TWINS-determined ion spectral shapes for a case study interval: 1130–1146 UT on 6 April 2010. The 5–6 April 2010 storm was triggered by the first coronal mass ejection (CME) of solar cycle 24 [*Connors et al.*, 2011], and the interval for this study was selected because (a) the viewing geometry was advantageous to capture LAEs from nightside ion precipitation and (b) the quality of the TWINS images was excellent, with low background levels.

[8] In section 2, we present geometrical calculations to determine the geophysical locations (MLT and magnetic latitude) and local pitch angles of TWINS limb pixels. In section 3, we apply our geometrical analysis to study the geophysical distribution of ENA emissions from our selected interval.

[9] In section 4 we use the thick-target approximation (TTA) of *Bazell et al.* [2010] to obtain ion spectra and employ a methodology similar, though not identical, to theirs (including pixel-averaged fluxes) to validate the ion spectra via comparison with simultaneous NOAA data from a similar magnetic latitude and roughly one MLT hour west of the TWINS-observed LAEs. We show that the determination of absolute ion flux bears a large uncertainty related to the fact that the TWINS pixels do not resolve the precipitation region, and thus, the degree of agreement between the TWINS and NOAA ion spectra depends greatly on which NOAA-observed precipitation feature is selected for comparison. We also demonstrate that geometrical correction of ENA differential flux (i.e., scaling the observed ENA flux by the ratio of the TWINS pixel size to the assumed angular size of the LAE source region) does not necessarily produce trustworthy values of absolute ion flux.

[10] We then (section 5) calculate TWINS ion spectra for individual pixels spanning several hours of MLT along the Earth limb. We show that the TWINS spectral shapes for our event are notably different than the monotonic,  $(\text{Energy})^{-1}$  dependence found for LAE-derived ions by *Bazell et al.* [2010]. The 6 April 2010 TWINS spectra exhibit a clear local time dependence favoring higher average energy near dusk than dawn, consistent with ion drift physics. This result depends not on the absolute value of the TWINS-estimated

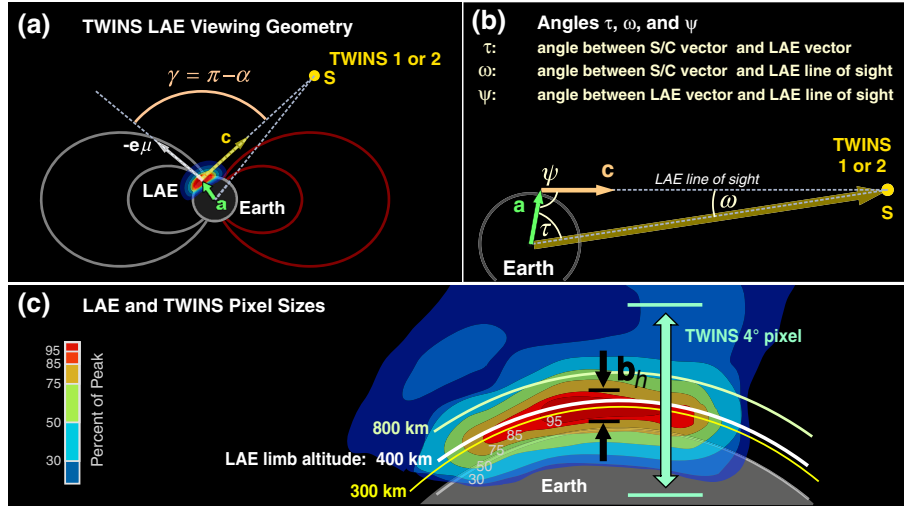


**Figure 1.** Viewing geometry for low altitude emission (LAE) signatures. Because of the highly directional emissivity function [Pollock *et al.*, 2009; Bazell *et al.*, 2010], a TWINS imager observes LAEs from the opposite limb, e.g., an imager on the dayside observes LAEs from the nightside limb. (a) The local pitch angle of the low-altitude ENAs is estimated as  $\cos \alpha = \mathbf{e}_\mu \cdot \hat{\mathbf{c}}$  (cf. text). (b) Definition of angles  $\tau$ ,  $\omega$ , and  $\psi$  used to derive LAE colatitude. (c) Contours of LAE intensity, depicting vertical scale height, adapted from a high-spatial-resolution Astrid ENA image [Brandt *et al.*, 2001a, 2005]. For comparison, the green double arrow indicates the radial size of a TWINS pixel from a vantage point  $\sim 6 R_E$  away.

ion flux, but rather upon the shapes of the individual pixel spectra. We find a weaker trend favoring hotter ions at more equatorward latitudes, most likely reflecting that the more energetic duskside ions are following drift trajectories closer to the Earth than the less energetic dawnside ions. The latitudinal correlation is less clear, perhaps owing to greater uncertainty in the geometric latitude determination.

[11] From these results, we show that TWINS ENA imaging can resolve MLT-dependent low-altitude ion spectral shape information simultaneously across a broad range of MLT and may resolve some of the latitudinal dependence. The ability to resolve pixel-to-pixel local-time-dependent spatial structure advances previous results that considered much coarser MLT structure via comparisons of two widely separated (in MLT) pixels, or averages of larger groups of pixels from the LAE region [e.g., Bazell *et al.*, 2010; McComas *et al.*, 2012]. Our result also augments previous statistical analysis of the local time dependence of ion spectra [Hardy *et al.*, 1989], by providing system-level information in a single image rather than in a sequence of temporally decorrelated single-point measurements.

[12] The observation of LAEs thus enables broad MLT coverage of magnetospheric ion precipitation, which can provide contextual and/or complementary spatial and spectral information for more local observations such as made by a variety of in situ spacecraft.

[13] In the next section we describe our analysis methodology.

## 2. Methodology

[14] In this section, we describe the geometrical calculations used to determine the geophysical locations (MLT and magnetic latitude,  $\Lambda$ ) and local pitch angles ( $\alpha$ ) of TWINS limb-viewing pixels, and our implementation of the thick

target approximation developed for LAE analysis by Bazell *et al.* [2010].

### 2.1. TWINS Viewing Geometry

[15] In this study, TWINS LAE emissions are sampled along or just inside the Earth's limb as seen from the viewing geometry depicted in Figure 1. The TWINS spacecraft (either 1 or 2) is at location  $\mathbf{s}$ , and the LAE is located at  $\mathbf{a} \equiv a\hat{\mathbf{r}}$ . Unit vector  $\hat{\mathbf{c}} \equiv d^{-1}(\mathbf{s} - \mathbf{a})$  points from the LAE to the TWINS spacecraft along the pixel line of sight (LOS), where  $d$  is the distance between the spacecraft and the LAE source location:

$$d = [r_s^2 + a^2 - 2\{\rho_s \rho_a \cos(\varphi_s - \varphi_a) + z_s z_a\}]^{\frac{1}{2}}. \quad (1)$$

Here we employ a mixture of standard Cartesian  $(x, y, z)$ , spherical  $(r, \theta, \varphi)$ , and cylindrical  $(\rho, \varphi, z)$  coordinates as convenient to simplify the mathematical form of our equations. Subscripts “s” and “a” refer to vectors  $\mathbf{s}$  and  $\mathbf{a}$ , respectively. The problem to solve is the following: given the spacecraft location  $\mathbf{s} = (r_s, \theta_s, \varphi_s)$ , determine the LAE geophysical location  $\mathbf{a} = (a, \theta_a, \varphi_a)$ .

#### 2.1.1. Radial and Azimuthal LAE Location

[16] In this study, the LAE is assumed to originate from an altitude  $h$ , i.e., geocentric distance  $a = R_E + h$ . We use  $h = 400$  km, based on high-spatial-resolution Astrid LAE observations taken from low altitude [Roelof and Skinner, 2000; Brandt *et al.*, 2001a, 2005], depicted in Figure 1c. Our determination of the LAE location is not very sensitive to the choice of LAE altitude because the angular size in the TWINS field of view (FOV) encompassed by scale size  $(a - R_E)$  is typically smaller than a TWINS pixel. From a TWINS spacecraft-to-LAE distance of  $6 R_E$ , scale sizes  $(a - R_E)$  ranging from 300 to 800 km are a factor of 3 to 9 times smaller than a  $4^\circ$  TWINS pixel, with the largest factor corresponding to the smallest  $h$ . However, as discussed later

(section 2.2), the choice of the related quantity  $b_h$ , the altitude thickness of the LAE, does affect the geometric scaling correction applied to the ENA differential flux.

[17] The azimuthal angle of the LAE,  $\varphi_a \equiv \pi(\text{MLT}_a - 12)/12$ , is determined numerically in the spherical “skymap” projection used to display TWINS images (cf. Figure 4). We project meridional lines (emanating from the SM coordinate pole) onto a sphere of radius  $a$ , at  $n_p$  evenly spaced azimuthal angles and calculate their intersections with the limb of that sphere, generating an array of  $n_p$  values of  $\varphi$  along the limb. Then for each TWINS limb pixel (cf. section 2.1.4), the value  $\varphi_a$  is assigned as that of the closest of the  $n_p$  points. We use  $n_p = 315$ , corresponding to one projected meridional line every  $\sim 4.5$  min of MLT, sufficient to well resolve the  $4^\circ$ -by- $4^\circ$  (instrument frame) TWINS pixels whose mean skymap-projected MLT-width is  $\sim 1$  h (cf. section 2.1.5). We note that the apparent MLT of the LAE is dependent upon the geocentric radius ( $a$ ) assumed for the LAE, but this is a small effect compared to the MLT width of each pixel.

### 2.1.2. LAE Colatitude

[18] To derive an expression for LAE magnetic colatitude,  $\theta_a = \pi/2 - \Lambda_a$ , we apply the law of cosines for the three angles depicted in Figure 1b:

$$d^2 = a^2 + r_s^2 - 2ar_s \cos \tau \quad (2)$$

$$a^2 = d^2 + r_s^2 - 2dr_s \cos \omega \quad (3)$$

$$r_s^2 = d^2 + a^2 - 2da \cos \psi \quad (4)$$

Setting equal  $d^2$  from (2) and (3), we obtain an equation for angle  $\tau$ , which is most similar to magnetic latitude  $\Lambda_a$  (and thus most closely related to colatitude  $\theta_a$ ), as a function of  $\omega$ , each LAE pixel’s angular offset from the origin:

$$\cos \tau = \frac{r_s}{a} - \frac{d}{a} \cos \omega. \quad (5)$$

The angle  $\omega$  is essentially the TWINS instrument’s imaging angle (corresponding to the instrument collimator direction; cf. section 2.1.5 and *McComas et al.* [2009a]), equal to  $n_\lambda \Delta\lambda$ , where  $\Delta\lambda (= 4^\circ)$  is the imaging-angle pixel resolution and  $n_\lambda$  is the number of imaging-angle pixels from the center of the Earth. Equation (5) for  $\cos \tau$  includes distance  $d$ , which in (1) depends on  $\theta_a$ , the quantity for which we are solving. To provide a solution which does not depend on prior knowledge of the LAE colatitude, we apply the quadratic formula to equation (3) and express distance  $d$  solely as a function of the imaging angle  $\omega$ :

$$d(\omega) = r_s \left( \cos \omega - \sqrt{(\cos^2 \omega - 1) + (a/r_s)^2} \right). \quad (6)$$

Here we have rejected the + solution which corresponds to the intersection of the LOS with  $r = a$  on the back side of the Earth, not visible to TWINS. With (5) and (6), we equate  $d^2$  of (1) and (2) to obtain

$$\cos \theta_a = [z_s^2 + \xi^2]^{-1} \left( z_s r_s \cos \tau - \xi \sqrt{z_s^2 + \xi^2 - r_s^2 \cos^2 \tau} \right) \quad (7)$$

where  $\xi \equiv \rho_s \cos(\varphi_s - \varphi_a)$ . We reject the + solution which corresponds to the Southern Hemisphere. For pixels located precisely at the limb,  $\psi_{\text{limb}} = \pi/2$ , equation (4) reduces to

$r_s^2 = a^2 + d^2$ , and equation (3) yields the angular size of the limb:

$$\cos \omega_{\text{limb}} = \frac{d}{r_s} = \sqrt{1 - \left(\frac{a}{r_s}\right)^2}. \quad (8)$$

Equation (2) then becomes  $\cos \tau_{\text{limb}} = a/r_s$ , yielding the limb solution

$$\cos \theta_{a,\text{limb}} = [z_s^2 + \xi^2]^{-1} \left( z_s a - \xi \sqrt{z_s^2 + \xi^2 - a^2} \right). \quad (9)$$

### 2.1.3. LAE Pitch Angle

[19] We estimate the local pitch angle ( $\alpha$ ) sampled from the TWINS vantage point as  $\cos \alpha = \mathbf{e}_\mu \cdot \hat{\mathbf{c}}$ , where  $\mathbf{e}_\mu$  is a unit vector in the direction of the dipole geomagnetic field:

$$\cos \alpha = -\frac{h_\mu}{a^3 d} \left\{ \frac{3}{2} \sin 2\theta_a (\xi - \rho_a) + (3 \cos^2 \theta_a - 1) \delta z \right\}, \quad (10)$$

where  $\delta z = (z_s - z_a)$ , and  $h_\mu = a^3 (1 + 3 \cos^2 \theta_a)^{-1/2}$  is the scale factor for the field-aligned dipole coordinate.

### 2.1.4. Limb Pixel Selection

[20] Because the TWINS imaging-angle pixel resolution  $\Delta\lambda$  ( $4^\circ$ ) is typically larger than the radial extent of the LAE source region, and because pixels are generally not perfectly aligned with the true LAE limb (at  $r = a$  or  $\omega = \omega_{\text{limb}}$ ), we must account for the deviation offset  $\Delta\omega \equiv \omega - \omega_{\text{limb}}$  of each pixel and use the general (non-limb) solution of equation (7). With some algebra, it can be shown that to satisfy the condition,  $\cos \theta_a \leq 1$  restricts the solution such that  $\omega \geq \omega_C$ , where

$$\cos \omega_C = \frac{r_s^2 - a z_s}{r_s \sqrt{r_s^2 - 2a z_s + a^2}}. \quad (11)$$

Thus, equation (7) provides a means of calculating the magnetic colatitude (and thus, latitude) of limb pixels in an annular region of the TWINS image, bounded above by the limb at  $r = a$  and below by angular offset  $\omega_C$ . In this study, we restrict our analysis to data for which the center of the pixel lies in this annular region of the image.

### 2.1.5. Uncertainty in MLT, Latitude, and Pitch Angle

[21] Each TWINS imager consists of two collimating sensor heads mounted on a rotating actuator that sweeps back and forth over an approximately Earth-centered viewing cone [*McComas et al.*, 2009a, 2012; *Valek et al.*, 2010]. Thus, the instrument’s 1-D imaging angle  $\lambda$  (parallel to the collimator plates) corresponds roughly to geophysical radius and the actuation angle corresponds approximately to geophysical longitude. Calculated values of MLT and magnetic latitude, assigned to the center of each pixel, bear an uncertainty associated with the finite size of TWINS pixels.

[22] For a truly Earth-centered TWINS image, and for an LAE in the same geophysical meridional plane as the TWINS spacecraft (i.e.,  $\cos(\varphi_s - \varphi_a) = \pm 1$ ), the imaging line of sight (LOS) projected onto a TWINS image would be normal to the projected limb curve at the point of intersection. In this ideal case, the MLT width of the LAE pixel would be  $\Delta\text{MLT} = 4^\circ$  ( $24/360$ )h  $\approx 0.3$ h. However, because the image is not quite centered on the Earth, and because imaging LOS are not generally normal to the limb curve, the average pixel’s MLT width is somewhat larger:  $\Delta\text{MLT} \approx 1$ h (cf. Figure 4b). The average uncertainty of the MLT value assigned to the center of the pixel is half the pixel width:  $\delta\text{MLT}_a \approx 0.5$ h. Note that apart from this pixel-related location uncertainty  $\delta\text{MLT}_a$ , there is an intrinsic minimum-scale

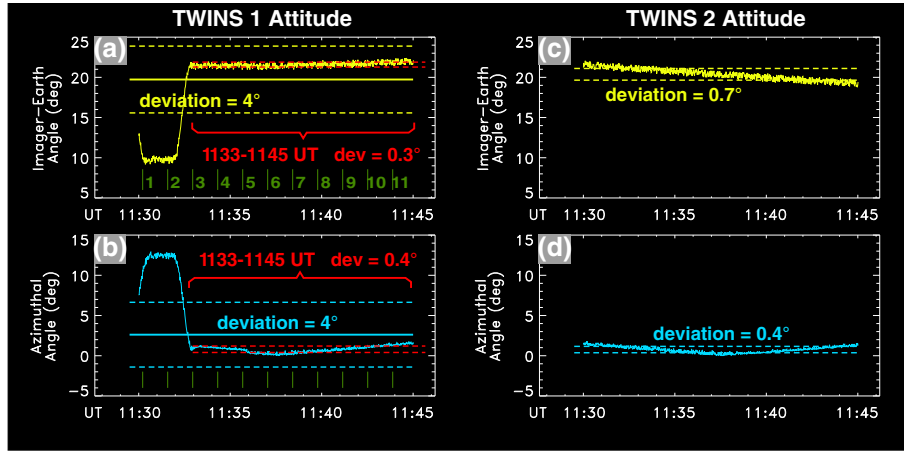


**Figure 2.** TWINS 1 and 2 attitude angles during 1130–1145 UT on 6 April 2010. (a) TWINS 1 imager-Earth angle, defined as the angle between the imager boresight and the unit vector pointing from the spacecraft to the Earth’s center. (b) TWINS 1 azimuthal angle, defined as the angular displacement in the plane normal to the imager boresight; displacement is measured relative to the orientation at the UT midpoint of the interval (i.e., 1138 UT). (c and d) Same as Figures 2a and 2b except plotted for TWINS 2. Individual actuation cycles during the 15 min integration time are numbered (1–11) for TWINS 1.

size of approximately 1 MLT h, smaller than which TWINS cannot resolve, because of the finite width of the slit camera (cf. section 5.5).

[23] Uncertainty in the LAE latitude  $\Lambda_a$  is much larger than that of MLT because LOS are tangential to the limb at the point of intersection (Figure 1a). With some algebra, the variation of latitude with imaging angle  $\partial\Lambda_a/\partial\omega$  can be computed from equation (7); its magnitude is infinite at the true limb and decreases with decreasing  $\omega$ . For a finite deviation offset  $\Delta\omega = \omega - \omega_{\text{limb}}$  where  $\omega > \omega_C$ , the magnitude of  $\partial\Lambda_a/\partial\omega$  is finite but still quite large. Our approach is to estimate the uncertainty  $\delta\Lambda_a$  as the difference in latitude between the pixel center ( $\omega_a$ ) and its inner edge:  $\omega_a - 0.5\Delta\lambda$ . Thus calculated for our study, the typical uncertainty is as much as several tens of degrees (cf. Figure 4c), which significantly decreases confidence in the absolute latitude of a given pixel. However, the pixel-to-pixel relative latitude may be meaningful for groups of pixels in a TWINS image (cf. section 5.4). Compounding the latitude uncertainty, the angular deviations  $\Delta\omega_a$  of the individual pixels produces a large scatter in  $\Lambda_a$ . Therefore, to quantify the effect of relative latitude, we use the average deviation  $\langle\Delta\omega_a\rangle = 1.2^\circ$  to calculate the values  $\Lambda_a$  assigned to the pixel centers and calculate the corresponding latitudinal uncertainties  $\delta\Lambda_a$  using the individual angular deviations  $\Delta\omega_a$  from the limb. These uncertainties  $\delta\Lambda_a$  are propagated through equation (10) to yield corresponding pitch angle uncertainties  $\delta\alpha_a$ .

### 2.1.6. TWINS Spacecraft Attitude

[24] In this study, each TWINS image is calculated by integrating ENA flux over a 15 min interval (i.e., approximately 11 sweeps of the rotating actuator). Though each TWINS spacecraft is an approximately nadir-pointing platform, adjustments in attitude that occur during the 15 min ENA integration can contribute to the uncertainty in the LAE location. Our plotted uncertainties (section 3) reflect only those associated with TWINS pixel size, but in this

section, we consider the quantitative effect of variable spacecraft orientation. Figure 2 plots the imager-Earth angle (top row) and azimuthal attitude angle (bottom row) for both TWINS imagers.

[25] First we discuss the attitude of TWINS 1. The imager-Earth angle is defined as the angle between the imager’s boresight [McComas *et al.*, 2009a] and the unit vector pointing from the spacecraft to the Earth’s center. This angle corresponds most closely to the instrument’s 1-D imaging angle  $\lambda$ . Thus, in terms of the uncertainties in position discussed in section 2.1.5, the imager-Earth angle contributes to latitudinal uncertainty in a manner quantitatively analogous to that of the  $4^\circ$  imaging-angle pixel size. Figure 2a shows that there was an  $\sim 12^\circ$  peak-to-peak attitude adjustment of the TWINS 1 spacecraft during the first two actuation cycles (i.e., prior to 1133 UT), after which time, the TWINS 1 attitude was stable to within a few tenths of a degree. For the entire 15 min interval, the TWINS 1 imager-Earth uncertainty is measured by the standard deviation, about  $4^\circ$ . Thus, the TWINS 1 uncertainties in latitude and pitch angle (plotted in section 3) that arise from the  $4^\circ$  pixel size must be scaled up by adding, in quadrature, the uncertainty associated with the  $4^\circ$  attitude deviation, i.e., these uncertainties must be multiplied by  $\sqrt{2}$  ( $= \sqrt{4^2 + 4^2/4}$ ). The azimuthal attitude angle plotted in Figure 2b is defined as the angular displacement in the plane normal to the imager boresight, and this angle corresponds to actuation angle. The  $4^\circ$  deviation in this azimuthal angle likewise increases the  $4^\circ$ -pixel-associated MLT uncertainty by a factor of  $\sqrt{2}$ . Overall, the TWINS 1 attitude adjustment during the first two actuator rotation cycles increases the uncertainties of latitude, pitch angle, and MLT each by approximately 41%.

[26] The TWINS 2 attitude was stable (to within several tenths of a degree) throughout the entire interval. The TWINS 2 imager-Earth angle deviation of  $0.7^\circ$  (Figure 2c) increases the latitude and pitch angle uncertainties each

by 2% ( $\sqrt{4^2 + 0.7^2}/4 = 1.02$ ). The TWINS 2 azimuthal attitude angle deviation of  $0.4^\circ$  (Figure 2d) increases the MLT uncertainty by half a percent.

[27] In summary, when the TWINS spacecraft are stable to within a degree or so, the contribution of spacecraft attitude to the uncertainties in LAE (or limb) location is negligible. However, when the TWINS image encompasses an attitude adjustment (such as that during 1130–1133 UT for TWINS 1), the contribution to the uncertainty in the LAE geophysical location can indeed be significantly increased. A strategy to minimize this uncertainty is to select intervals that do not include large attitude adjustments, where possible.

## 2.2. Geometric Flux Correction

[28] As mentioned in section 2.1.1, the vertical (i.e., with altitude) scale size of the LAE is significantly smaller than the  $4^\circ$  TWINS imaging-angle pixel can resolve. Assuming an LAE-scale size  $b_h$  (in km), the angular size in the TWINS imaging-angle direction of an LAE within the region  $1 R_E \leq r \leq (1 R_E + b_h)$  is (using equation (8))

$$\Delta\omega_{\text{LAE}} = \cos^{-1} \sqrt{1 - \left(\frac{R_E + b_h}{r_s}\right)^2} - \cos^{-1} \sqrt{1 - \left(\frac{R_E}{r_s}\right)^2}. \quad (12)$$

Although (12) assumes the altitude midpoint of the LAE region lies at  $r = R_E + b_h/2$ , the magnitude of this angular size  $\Delta\omega_{\text{LAE}}$  is the same if the midpoint is displaced in altitude. Because the TWINS imaging-angle pixel resolution  $\Delta\lambda$  is larger than  $\Delta\omega_{\text{LAE}}$ , the apparent LAE brightness in a TWINS pixel will be smaller than the true brightness by a factor  $F_c^{-1}$ , where

$$F_c = \Delta\lambda / \Delta\omega_{\text{LAE}}. \quad (13)$$

Therefore, in this paper, we apply a geometric correction to the LAE differential flux:

$$J_{\text{corrected}} = J_{\text{apparent}} \cdot F_c. \quad (14)$$

[29] This geometric flux correction attempts to account for the known mismatch in vertical LAE-scale size and TWINS imaging-angle pixel resolution. From Figure 1c, it can be expected that  $b_h$  might range from roughly 300 km to 800 km, depending on the precipitating ion flux, and what fraction of the peak is included in the definition (e.g., half-maximum). For TWINS imager location  $a = 6 R_E$ , this range (300–800 km) of  $b_h$  corresponds to values of  $F_c$  from 8.7 to 3.3 (respectively). In this study we use  $b_h = 300$  km, which corresponds to  $F_c = (8.66, 8.16)$  for (TWINS 1, TWINS 2), and which yields reasonable though not perfect agreement with NOAA data depending upon the closeness of the NOAA-TWINS conjunction (cf. section 4).

[30] The correction factor of (13) assumes a “side-view” of emissions above  $1 R_E$ , similar to that depicted in Figure 1c. This assumption may not be generally valid for TWINS LAE imaging. The emissivity functions of *Bazell et al.* [2010] were calculated only for sources inside the  $1 R_E$  limb, but preliminary calculations including emissions above  $1 R_E$  (E. C. Roelof, private communication, 2012) indicate two things. First, the brightest emission can often occur inside the  $1 R_E$  limb. Second, because the flux of emergent ENAs along a given LOS results from a chain of multiple charge exchange and stripping collisions, it may

not be possible to formulate a robust geometric correction that scales with the ratio of the TWINS pixel angular size to the angular size of the LAE emission region. In any case, the side-view geometry assumption would only be approximately valid for pixels containing the LAE limb ( $r = a$ ) within their field of view, i.e., for  $|\Delta\omega| = |\omega - \omega_{\text{limb}}| \leq \Delta\lambda/2$ . For TWINS imaging angle resolution  $\Delta\lambda = 4^\circ$ , this means the correction is valid for pixels inside the limb, offset by  $\leq 2^\circ$ . In principle, pixels offset by more than  $2^\circ$  could be corrected by factoring out the emissivity function of *Bazell et al.* [2010] (cf. section 3.1.2), which decreases as one moves farther inside the limb. In this study, we apply the limb-based geometric correction to all LAE pixels that satisfy the validity criterion  $\Delta\omega \leq 2^\circ$ , with the following rationale. First, we do not have available an analytical expression for the emissivity function to correct the flux for pixels inside the limb. (The emissivity function of *Bazell et al.* [2010] is calculated numerically.) Second, the geometric correction provides a slightly less arbitrary correction factor than the normalization constant of *Bazell et al.* [2010] (cf. section 2.3). Finally, though we perform a quantitative validation of the absolute magnitude of TWINS-measured LAE differential flux (section 4), our main results and conclusions (section 5) are dependent more upon the shape of the TWINS low altitude spectra than the absolute magnitude.

[31] The geometric correction does not account for MLT variation of the source fluxes smaller than the TWINS pixels or slit camera aperture can resolve (cf. sections 2.1.5 and 5.5). Even including the geometric correction, the brightness of an LAE pixel will be a convolution of the actual brightness of the LAE, the geophysical latitudinal dependence of the emissivity function *Bazell et al.* [2010], and the TWINS instrument response to angular scattering caused by ENAs passing through the carbon foils used in the TWINS cameras [*McComas et al.*, 2009a; *Funsten et al.*, 1993]. Regarding this last factor, Appendix A contains a brief consideration of the effect of foil scattering on a TWINS imager’s ability to resolve MLT structure in LAEs.

## 2.3. LAE Thick-Target Approximation (TTA)

[32] Through comparison of TWINS ENA images with ion data from the DMSF multi-spacecraft mission, *Bazell et al.* [2010] validated the thick-target approximation (TTA) analysis that allows LAEs to be used as a quantitative diagnostic of the broad global dynamics of ion precipitation. There are some important limitations to the TTA approach. First, TWINS pixels do not properly resolve the precipitation region, which is known (from in situ observations) to be highly spatially structured. Because of this limitation, TTA analysis can only capture precipitating ion dynamics on broader spatial scales, commensurate with TWINS pixel sizes. In our study, we show that one can resolve the global local time dependence with an intrinsic spatial scale of about 0.5–1 MLT h (cf. section 5). Another limitation arises from the finite width of TWINS energy bins. For precipitating ion spectra that are steeply falling (with energy), ENA flux within a given energy bin tends to be weighted toward lower energy, and this effect becomes more pronounced with increasing width of the energy bin. At higher energies, where fluxes are lower, energy bins may be wider to obtain sufficient counts for a healthy signal to noise.

**Table 1.** Coefficients of Fit  $\log_{10} \sigma = C_0 + m \Xi + f_0 \Xi^n \sin \left[ \pi \frac{\Xi}{E_1} \right]$  (with  $\Xi \equiv \log_{10} E$ ) to Charge Exchange ( $\sigma_c$ ) and Stripping ( $\sigma_s$ ) Cross Sections of *Basu et al.* [1987]

Coefficient	$\sigma_c$	$\sigma_c$	$\sigma_s$
	1–30 keV	30–1000 keV	1–1000 keV
$m$	−0.159	−0.695	0.04097
$C_0$	−15.30	−15.30	−16.00
$f_0$	0.	0.58	0.40
$E_1$	1.	2.425	2.9856
$n$	0.	1.	0.40

(In section 4, we use the overlap of the highest TWINS energy bin with the lowest NOAA energy bin to mitigate this concern.) Despite these limitations, the TTA approach was shown by *Bazell et al.* to yield ion spectral shapes (fundamental diagnostics of the ion precipitation process) that agree well with simultaneous in situ data.

[33] It is important to note that the TTA works only if the LAE intensity is not changed by the emissivity function, both in energy and space. Therefore, the TTA approach cannot be applied everywhere along the limb, but rather must be limited to the brightest portion of LAEs. We therefore restrict our analysis to pixels with at least 30% of the peak value.

[34] The TTA analysis of *Bazell et al.* [2010] provides a relation between the pixel-averaged (i.e., averaged over pixel solid angle) ENA differential flux  $\langle J_{\text{ENA}} \rangle$  and the precipitating ion source  $\langle J_{\text{ion}} \rangle$ :

$$\langle J_{\text{ion}} \rangle = N \left[ 1 + \frac{\sigma_s}{\sigma_c} \right] \langle J_{\text{ENA}} \rangle, \quad (15)$$

where  $\sigma_s$  and  $\sigma_c$  are the stripping and charge exchange cross sections, and  $N$  is a normalization factor manually adjusted by *Bazell et al.* to achieve agreement between TWINS and DMSP ion spectra at 5 keV. In our analysis, we test the validity of the geometric correction by equating  $N$  of *Bazell et al.* with our factor  $F_c$ . Their values of  $N$  ranged from 1.2 to 9.15, which according to equations (12) and (13) (and using their TWINS spacecraft locations  $r = 5.86$  and  $r = 6.18$ ,

respectively) correspond to LAE-scale sizes of 2300 km and 280 km. Given the uncertainties (and the unknown LAE-scale size which must be assumed in our analysis), the range of normalization factors  $N$  found by *Bazell et al.* is broader, but not inconsistent with the  $F_c$  we use in our analysis. However, as discussed in section 4.2.3, the high latitudinal uncertainty prevents a definitive validation of the geometric correction factor  $F_c$ . It is also possible that the factor  $F_c$  is energy dependent, although *Bazell et al.* interpreted the good agreement in TWINS and DMSP spectral shapes as evidence against this possible energy dependence.

[35] To use equation (15) to convert ENAs to ions requires an expression for the energy-dependent charge exchange cross sections; we use the following fit to the  $\sigma$  values of *Basu et al.* [1987]:

$$\log_{10} \sigma = C_0 + m \Xi + f, \quad (16)$$

where the function  $f$  is given by

$$f = f_0 \Xi^n \sin \left[ \pi \frac{\Xi}{E_1} \right], \quad (17)$$

and  $\Xi \equiv \log_{10} E$  is the base-10 logarithm of energy. Our coefficients of the fit for the charge exchange ( $\sigma_c$ ) and stripping ( $\sigma_s$ ) cross sections are given in Table 1. The ad hoc fit for  $\sigma_c$  has a discontinuous derivative at 30 keV. The cross sections  $\sigma_c$  and  $\sigma_s$  are plotted in Figure 3b.

[36] We note one fine point related to TWINS energy binning. The energy bins are 100% wide, i.e., each TWINS energy bin  $E_j$  includes flux from  $0.5E_j$  through  $1.5E_j$ . When using the TTA method, we calculate the energy-dependent coefficient  $J_c \equiv (1 + \sigma_s \sigma_c^{-1})$  contained in equation (15) and plotted in Figure 3a. In our analysis, we use the value of  $J_c$  at the center value ( $E_j$ ) of each TWINS energy bin. An alternate approach might be to average the function  $J_c$  over each energy bin; doing so results in values of  $J_c$  that differ by under 3% from the values we use (minimum difference: 0.2%, at 16 keV; maximum difference: 2.6%, at 50 keV; mean difference: 1%).

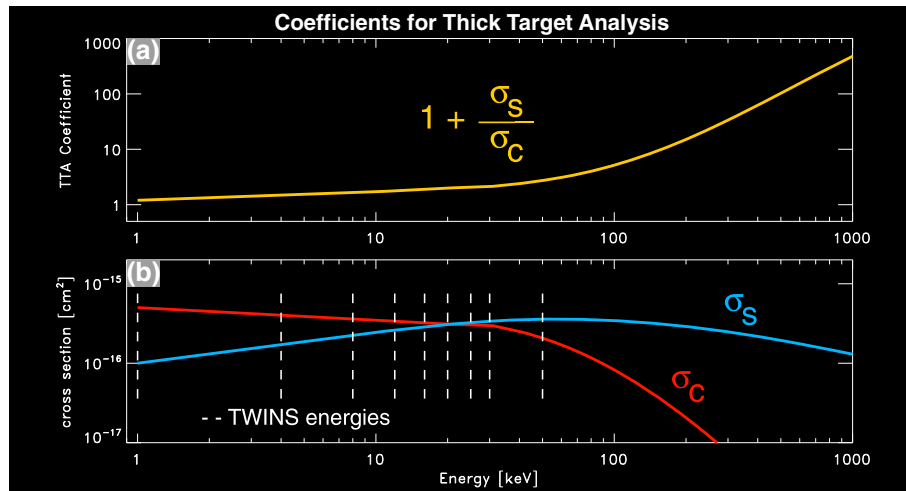


**Figure 3.** Coefficient and cross sections for thick target analysis (TTA). (a) Dimensionless coefficient  $(1 + \sigma_s \sigma_c^{-1})$  from equation (15). (b) Charge exchange ( $\sigma_c$ ) and stripping ( $\sigma_s$ ) cross sections, estimated using equation (16) and coefficients in Table 1; see text.

## 2.4. Implementation of TTA

[37] A component of our analysis uses a simplified implementation of the thick target approximation (TTA) of *Bazell et al.* [2010] to obtain ion spectra from the low-altitude ENA measurements. The TTA method calculates an emission source region using an analytical approximation for the multiple charge-exchange and stripping collisions occurring in the optically thick oxygen exobase. The apparent LAE brightness, as viewed from a particular vantage point, is then calculated via a numerical line-of-sight integration through the model emission source region. Since the parent ion distribution is unknown, *Bazell et al.* [2010] assumed an idealized (spatially uniform) ion distribution to calculate a viewing-geometry dependent “emissivity function” (section 3.1.2). Used together with the emissivity function, equation (15) can in principle recover the absolute ion flux from the precipitation region.

[38] In this paper, we circumvent the numerical calculation of the emissivity function and apply equation (15) to a geometrically corrected ENA flux (cf. section 2.2). The goal is to determine what information can be obtained with a simplified version of the TTA approach. We show that our simplified approach with its set of approximations does yield useful quantitative information about the source ion distribution.

[39] In the rest of this paper, we apply our methodology to TWINS imaging data from a 15 min interval of strong LAEs during 6 April 2010.

## 3. TWINS Observations

[40] Figure 4 shows TWINS data from the 15 min ( $\pm 1$  min) interval 1130–1146 UT during the weak ( $-73$  nT) CME-driven geomagnetic storm of 6 April 2010 [*Connors et al.*, 2011; *McComas et al.*, 2012; *Buzulukova et al.*, 2012; *Goldstein et al.*, 2012a, 2012b]. The first row (Figure 4a) contains 30 keV TWINS 1 and TWINS 2 images in the left and right columns, with the LAE signature indicated in each image. The second to fourth rows (Figures 4b–4d) show ENA differential flux sampled along the limb, plotted versus values of MLT, magnetic latitude ( $\Lambda$ ), and pitch angle at (or near) the limb.

### 3.1. MLT Distribution of LAEs

[41] During this interval, the TWINS 1 averaged location (in SM coordinates) was  $(r_s, \text{MLT}_s, \Lambda_s) = (5.9 R_E, 1208, 56^\circ)$ , and TWINS 2 was at  $(5.6 R_E, 1035, 59^\circ)$ . That is, the two imagers were at similar radii and latitude and separated by 1.5 h of local time. This stereo-viewing geometry, in which the two imagers’s perspectives differ mostly by MLT, is in principle useful for determining whether there is an MLT boundary in the ion precipitation.

#### 3.1.1. Extent of MLT Distribution

[42] Figure 4b depicts the LAE flux versus MLT. The dots are the flux values of individual limb pixels, color coded using the same color bar as the TWINS images. Vertical and horizontal bars at each dot indicate the uncertainties in differential flux and MLT, respectively. The MLT uncertainties were discussed in section 2.1.5. (Note that the TWINS 1 MLT bars must be multiplied by  $\sqrt{2}$  to include the effect of attitude variations during 1130–1133 UT; cf. section 2.1.6.) The vertical bar at each flux dot is a combination (added

in quadrature) of the Poisson counting error and the scatter from a running average 0.5 MLT h in width. The scatter from the running average is meant to measure the magnitude of unphysical fluctuations with scale sizes smaller than the MLT uncertainty (cf. section 2.1.5).

[43] TWINS 1 and 2, imaging the same ion precipitation region from slightly different vantage points (approximately 1.5 MLT h apart), see somewhat different MLT distributions. The solid curve is a fit to the pixel data using a two-component Gaussian:

$$G_f = \sum_{i=0,1} C_i \left\{ A_{i0} + A_{i1} \exp \left[ -\frac{1}{2} \left( \frac{\varphi - A_{i2}}{A_{i3}} \right)^2 \right] \right\}, \quad (18)$$

where  $C_i = (0.4, 0.7)$ , and the coefficients  $A_{ij}$  are

$$\text{TWINS 1 : } \begin{aligned} A_{0j} &= (0.016, 0.23, 2.57, 0.17) \\ A_{1j} &= (0.016, 0.11, 3.05, 0.66) \end{aligned} \quad (19)$$

$$\text{TWINS 2 : } \begin{aligned} A_{0j} &= (0.009, 0.12, 2.63, 0.44) \\ A_{1j} &= (0.010, 0.10, 2.73, 0.59) \end{aligned} \quad (20)$$

The Gaussian fits are included both to guide the eye and provide a quantitative metric of the flux-versus-MLT distribution. A two-component fit is performed to account for two possible MLT-scale sizes, i.e., to determine if there is a narrower peak embedded in a broader MLT distribution. The first component (index  $i = 0$ ) models the more localized peak, if there is one. The second component ( $i = 1$ ) models the broader peak, and it is obtained by fitting a Gaussian function to a six-point boxcar average of the flux versus MLT. The MLT-scale size of the peak (i.e., the  $1/\exp$  MLT half-width of the peak) is  $W_{\text{MLT}} = 12\sqrt{2}A_{i3}/\pi$ . For TWINS 1, there is indeed a narrow peak ( $A_{03} = 0.17$ ,  $W_{\text{MLT}} = 0.9$  h), centered at 2149 MLT, embedded in the broader ( $A_{13} = 0.66$ ,  $W_{\text{MLT}} = 3.6$  h) distribution. For TWINS 2, the coefficients  $A_{0j}$  and  $A_{1j}$  are all very similar and indicate the absence of a narrow peak. The respective absolute peak fluxes occur at 2149 MLT and 2203 MLT for TWINS 1 and 2.

[44] Aside from consideration of the narrower peak in the TWINS 1 distribution, both TWINS 1 and 2 distributions contain LAE fluxes spanning a broad range of MLT. To characterize the MLT distribution in Figure 4b, vertical dotted lines are drawn where the fit equals 20% of its peak flux value. By this measure, the TWINS 1 LAE, spanning 1911–0403 MLT (09 h 14 min of local time), is approximately 50 MLT min broader than that of TWINS 2, which spans 1807–0231 MLT (08 h 24 min).

#### 3.1.2. Emissivity Function

[45] Because LAEs are produced by ions mirroring at low altitudes, the ability to image them is highly dependent on viewing geometry [*Roelof and Skinner*, 2000; *Pollock et al.*, 2009]. *Bazell et al.* [2010] used TTA analysis to calculate the emissivity function, which describes the portion of the TWINS FOV for which the viewing geometry favors LAE imaging. Conceptually, the emissivity function is an “artificial LAE emission pattern” calculated by assuming an ion precipitation region distributed uniformly in MLT and magnetic latitude and computed for a specific imager-viewing geometry. Consistent with prior observations, *Bazell et al.* found that the calculated emissivity function is a crescent-shaped region (hereinafter denoted the

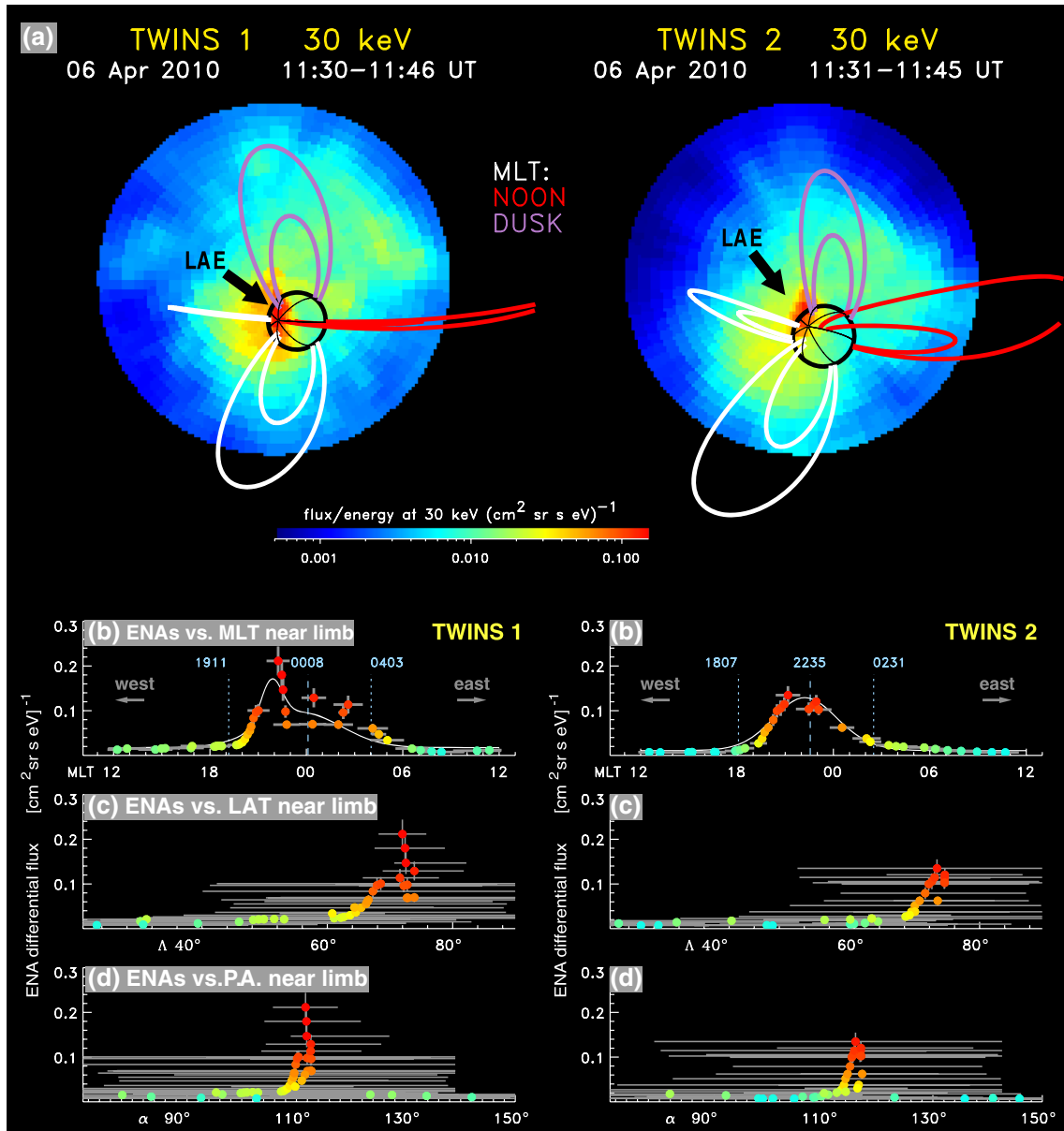


**Figure 4.** TWINS 1 and 2 images of low altitude emission (LAE), 6 April 2010, 1130–1146 UT ( $\pm 1$  min). The LAE signature spans a broad range of nightside MLT, and its peak is at the maximum latitude or pitch angle sampled along the limb. (a) Each image gives ENA flux intensity. Earth (center circle) and fiducial dipole field lines (at  $L = 4$  and  $8$ , color coded by MLT) drawn. The LAE is the brightest signature found at or near the Earth limb. (b–d) ENA intensity versus magnetic local time (MLT), latitude ( $\Lambda$ ), and pitch angle ( $\alpha$ ) along the limb. Note large uncertainties in  $\Lambda$  and  $\alpha$  at lower latitudes, where pixel LOS are nearly tangential to the limb.

“emissivity crescent”) at or within the limb on the far side of the Earth from the imager, centered roughly 12 MLT h (or  $180^\circ$  longitude) away from the imager’s location. Furthermore, the brightness of the emissivity function peaks at  $\sim 180^\circ$  relative longitude and falls off with relative longitude in either direction. (There is also a gentler roll-off with increasing latitude away from the limb.) In the idealized case of two imagers whose locations differ only by MLT, the emissivity functions for the two imagers would be identical except for a constant MLT offset. *Bazell et al.* used comparison of the emissivity function to the observed LAE’s MLT

distribution to identify edges in ion precipitation. Here we attempt to use this method.

[46] In Figure 4b, dashed lines 12 MLT h away from the TWINS 1 and 2 imagers mark the limb location directly opposite to each imager. The TWINS 1 line is 1.5 MLT h east of the TWINS 2 line. In the idealized case where ion precipitation is uniformly distributed in local time, the MLT widths of the LAE distributions for TWINS 1 and 2 would be the same, but the TWINS 1 distribution would be shifted 1.5 MLT h east of that of TWINS 2. However (as stated above), the TWINS 2 distribution is actually approximately

50 min narrower: whereas the TWINS 1 and 2 eastern edges are indeed offset by  $\sim 1.5$  MLT h, the TWINS 1 western edge is only  $\sim 1$  MLT h east of the TWINS 2 western edge. Taken at face value (and assuming the idealized case), this would indicate that there is a real edge in the MLT distribution of ion precipitation at 1807 MLT, the location of the TWINS 2 edge. However, without actually calculating the emissivity function, and considering the uncertainties in both the Gaussian fits and in the MLT determination, we cannot determine conclusively that this western LAE edge at 1807 MLT is an ion precipitation edge. Based on the as-expected 1.5 h shift in the TWINS 1 versus TWINS 2 eastern LAE edges, we conclude that these eastern edges are almost certainly caused by the longitudinal dependence of the emissivity function. Thus, setting aside the possibility that the western LAE edge seen by TWINS 2 might coincide with an MLT boundary in ion precipitation, the broad MLT distributions seen by TWINS 1 and 2 correspond to the LAE emissivity crescents (as defined by *Bazell et al.* [2010]) visible to the two imagers.

### 3.2. Latitude and Pitch Angle Dependence

[47] Figure 4c plots LAE differential flux versus magnetic latitude ( $\Lambda_a$ ), calculated using equation (7). As described in section 2.1.5, we use the average deviation from the true limb ( $\Delta\omega_a$ ) =  $1.2^\circ$  to calculate the values of  $\cos\omega_a$  in equation (5), and thus determine the values  $\Lambda_a$  assigned to the pixel centers, plotted as the color-coded dots. We use the individual angular deviations of each pixel  $\Delta\omega_a$  to calculate the corresponding latitudinal uncertainties  $\delta\Lambda_a$ , plotted as the horizontal bars. (Note that the plotted latitudinal uncertainties for TWINS 1 must be multiplied by  $\sqrt{2}$  to include the effect of varying spacecraft attitude during 1130–1133 UT; cf. section 2.1.6) Although the uncertainties are tens of degrees wide, they show a clear trend because the uncertainty lies not in the calculated location but rather arises from the lack of knowledge about where in the latitudinal pixel the real emission occurred. The dependence of flux versus  $\Lambda_a$  is not single valued, but increases to a maximum at  $\sim 74^\circ$  for both TWINS 1 and 2. This trend results purely from the viewing geometry; for an Earth-pointed imager in a Molniya orbit, pixels near the limb will follow just such a non-single-valued curve versus latitude. Note also that the peak flux value occurs close to the peak latitude; this attribute results from geometry as well; the peak near-limb latitude will occur at the location  $180^\circ$  in longitude away from the imager, i.e., near the peak in the emissivity function. This clear trend indicates that though the absolute magnetic latitude of an individual pixel cannot be precisely determined, the relative latitude between adjacent pixels do follow a trend that can be used to discern dependence on changes in latitude along the limb. Note also that for the highest latitude TWINS 1 pixels, the latitude uncertainty bars are significantly smaller than at lower latitude; these pixels have slightly larger individual pixel offsets from the true limb, which reduces the uncertainty as discussed in section 2.1.5.

[48] In Figure 4d, the LAE differential flux versus the geometric pitch angle of equation (10) is plotted. The horizontal bars give the pitch angle uncertainty  $\delta\alpha_a$ , plotted by propagating the  $\delta\Lambda_a$  above through equation (10). The LAEs emerge from the source region in a narrow range of

pitch angle, peaking at  $112^\circ$  for TWINS 1 and  $116^\circ$  for TWINS 2. These pitch angles describe particles that are nearly mirroring in the exobase and are not inconsistent with the LAE pitch angle range of  $98^\circ \pm 15^\circ$  found by *Pollock et al.* [2009]. Given the large uncertainties, the fact that the TWINS 1 and 2 fluxes have peak-value pitch angles that differ by  $\sim 4^\circ$  is probably not geophysically meaningful.

### 3.3. ENA Intensity Outside the Limb

[49] Though we have restricted our geometric analysis to pixels at or just inside the limb (cf. section 2.1.4), there is comparable ENA flux well outside (i.e., 2–3 pixels outside) the  $r = a$  limb. For the 30 keV images shown in Figure 4, this is very probably not scattering in the instrument foils (cf. section A), but rather reflects parent ions at small pitch angles, i.e., whose bounce motion along the field line takes them down to near-limb altitudes. In support of this assertion, while TWINS 1 sees bright (i.e., orange) ENA emissions extending beyond the dawnside limb, TWINS 2 does not; if the pixels outside the dawnside limb were caused by foil scattering, both instruments would see this effect. Thus, in addition to providing geophysically useful information, in this case stereo imaging also helps rule out the possibility of an instrumental artifact. Note also the extension beyond the duskside limb, which coincides with the radial direction in the circular TWINS image; at 30 keV, this signature likely comes from counts of geophysical origin (i.e., from small pitch angles). The linear-like feature is exaggerated by the mapping from the rectangular instrument (imaging-angle-versus-actuation-angle) coordinates to the circular “skymap” image coordinates, because near the center of the image, there is a singularity in the skymap coordinate system.

### 3.4. Energy Dependence

[50] Figure 5 plots ENA differential flux of limb pixels versus MLT, magnetic latitude, and pitch angle, for nine energy bins from 1 keV to 50 keV. Each energy bin  $E_j$  integrates ENA counts (which are converted to differential flux) from  $\pm 0.5E_j$ , e.g., the 1 keV bin spans 0.5–1.5 keV, the 4 keV bin spans 2–6 keV, and so on. ENA fluxes generally decrease with increasing energy. In the dusk MLT sector (west of midnight), however, the ENA flux intensity flattens out at lower energies, decreasing to a local minimum at the lowest energy bin (1 keV, gray curve). The general spatial dependencies noted for 30 keV fluxes (in sections 3.1 and 3.2) hold for all energies, although the range of MLT spanned by the LAE narrows and shifts duskward at the highest energies. For example, the 50 keV flux-versus-MLT curve (red curve) falls more rapidly with MLT east of midnight than does the 1 keV (gray) curve. This duskward shift with increasing energy is qualitatively consistent with ion drift physics: lower energy ions act under the influence of both an eastward  $E \times B$  drift and a westward magnetic gradient-curvature drift, whereas higher-energy ion drifts are dominated by westward magnetic drift.

## 4. TWINS and NOAA Conjunction

[51] Through comparison of TWINS ENA images with ion data from the DMSP multi-spacecraft mission, *Bazell et al.* [2010] validated the thick-target approximation (TTA)

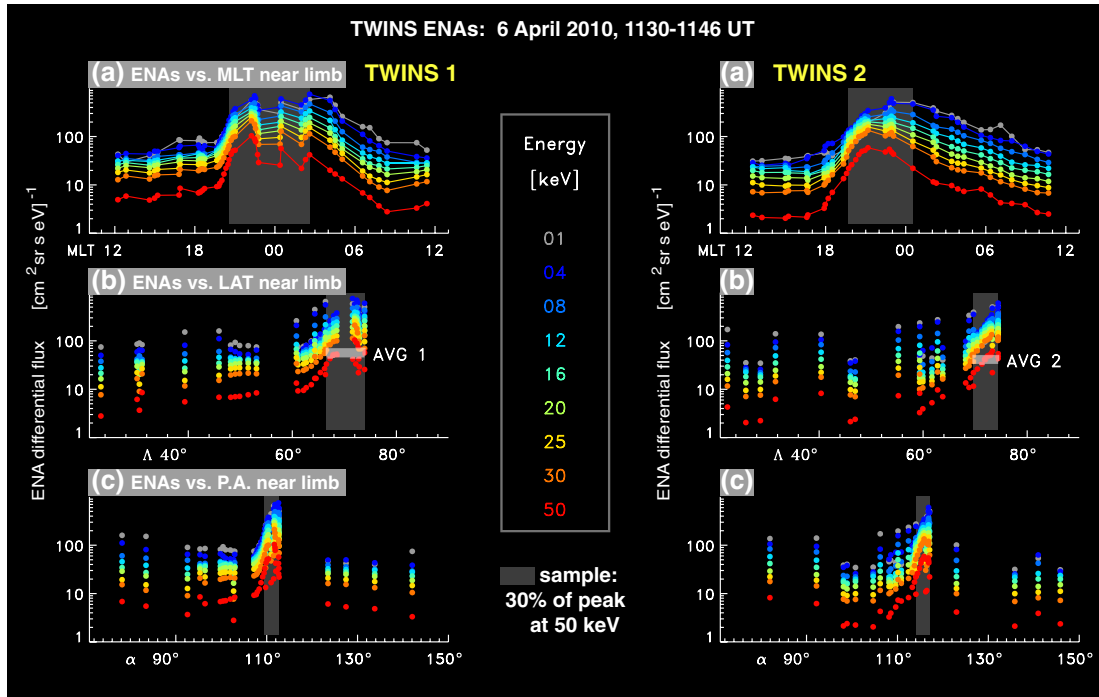


**Figure 5.** TWINS observations on 6 April 2010, 1130–1146 UT, of ENA intensity of limb pixels versus (a) MLT, (b) latitude, and (c) pitch angle for TWINS energy bins from 1 keV to 50 keV. The gray boxes indicate pixels for which the 50 keV channel intensity is  $\geq 30\%$  of the peak value at 50 keV; these pixels are selected for comparison with NOAA data. The horizontal bar in the latitude plot gives the average of the selected 50 keV pixels.

analysis that allows LAEs to be used as a quantitative diagnostic of the broad global dynamics of ion precipitation. In this section, we adapt the TTA validation method to a TWINS-NOAA conjunction study, as follows. We convert TWINS ENAs into ion differential fluxes, which are compared with the proton fluxes of NOAA during a conjunction of the three spacecraft (TWINS 1 and 2, and NOAA 17). The ion fluxes from TWINS and NOAA are combined to produce a low-altitude ion spectrum spanning 0.5–800 keV.

#### 4.1. NOAA/POES Precipitating Protons

[52] The orbits of the NOAA/POES satellites are polar and sun-synchronous at an altitude of about 850 km and with an orbital period of 100 min. The orbits of the different satellites cover different local times. The instrument used in this study is the Medium Energy Proton and Electron Detector (MEPED) which provides directional measurements of energetic protons and electrons at pitch angles of  $0^\circ$  and  $90^\circ$ . In this study, particles in three energy ranges are used: 30–80 keV, 80–240 keV, and 240–800 keV. The detectors are sensitive to both protons and neutral particles, but give neither mass resolution nor the charge state of the particles. Though the term protons is used throughout this paper, MEPED cannot distinguish between different ion species. For a discussion of the instrument response to heavier ions, see *Søråas et al.* [2002].

[53] Figure 6 shows NOAA 17 MEPED proton measurements by the vertical and horizontal detectors on the satellite, from 6 April 2010 during the time interval 1130–1146 UT of TWINS imaging observations

(cf. Figures 4 and 5. The left column plots  $0^\circ$  pitch-angle protons versus MLT, magnetic latitude (LAT) and UT. The right column plots  $90^\circ$  pitch angles. All of the NOAA observations shown are from the Northern Hemisphere. As indicated by the color legend in the center, protons in three energy ranges (30–80, 80–240, and 240–800 keV) are shown. From the plots, the region of proton precipitation and the proton energy spectrum can be determined. Qualitatively, the flux decreases sharply with energy for all NOAA-observed protons in this interval. NOAA’s polar orbit obtained roughly meridional slices through two distinct bands of intensified proton precipitation, labeled “A” and “B” in the  $90^\circ$ -pitch-angle data of Figure 6. Precipitation band A fell within roughly 1900–1920 MLT and a latitude range of  $58^\circ$ – $66^\circ$ . Precipitation band B fell within 1805–1825 MLT and  $68^\circ$ – $72^\circ$ . NOAA observed higher fluxes in A, the more eastward and equatorward band.

#### 4.2. TWINS-NOAA Comparison

[54] In this section, we compare TWINS ion differential fluxes (converted from ENAs using TTA analysis) to NOAA proton fluxes. Because the highest energy bin of TWINS ( $50 \text{ keV} \pm 25 \text{ keV}$ ) is nearly identical to the lowest NOAA energy bin (30–80 keV), a TWINS-NOAA conjunction study offers a good opportunity to validate our simplified implementation of the TTA method.

[55] To obtain a meaningful comparison between the TWINS ENA and NOAA proton measurements requires some care. Ideally, we would seek an exact conjunction during the 1130–1146 UT TWINS imaging interval, such

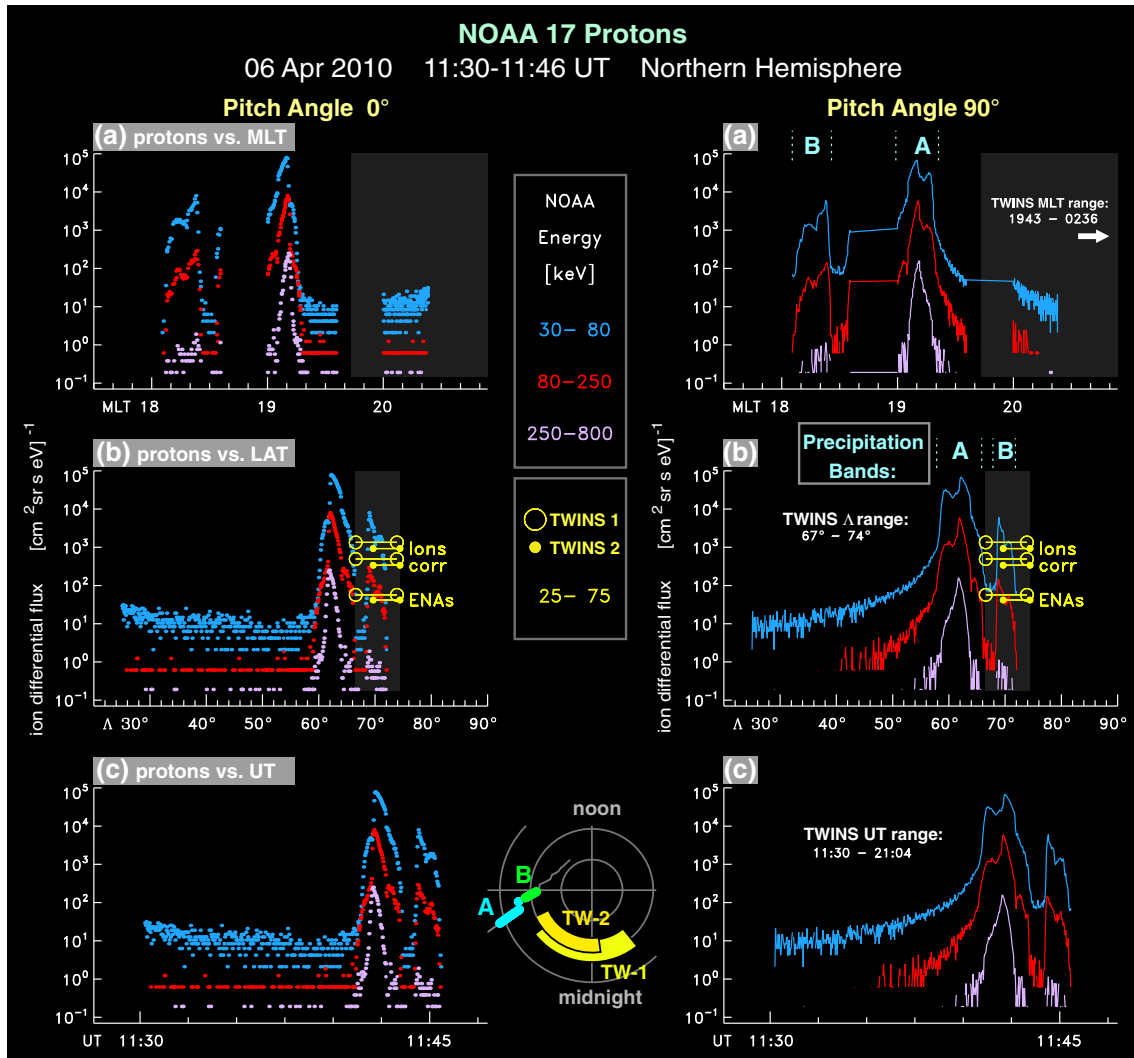


**Figure 6.** NOAA 17 MEPED proton measurements during 1130–1146 UT on 6 April 2010 by vertical (pitch angle  $0^\circ$ ) and horizontal (pitch angle  $90^\circ$ ) detectors, for three energy ranges: 30–80 keV, 80–240 keV, and 240–800 keV. Data are plotted versus (a) MLT, (b) latitude, and (c) UT. NOAA observed two distinct precipitation bands: A (1900–1920 MLT,  $58^\circ$ – $66^\circ$ ) and B (1805–1825 MLT,  $68^\circ$ – $72^\circ$ ). The average 50 keV intensities of the selected TWINS 1 and 2 pixels (from Figure 5b) are plotted (labeled “ENAs”), along with their geometrically corrected intensities (corr) and TTA-derived ion intensities (Ions). The polar dial plot at bottom center indicates the spatial relationship among NOAA bands A and B, and TWINS 1 and 2 LAE intervals.

that NOAA 17 sampled the proton precipitation oval at ranges of MLT and latitude corresponding to the strongest TWINS-observed LAE flux. However, NOAA 17’s polar orbit sampled precipitating protons mostly westward of the TWINS-observed LAE emissivity crescent. Therefore, given NOAA’s polar orbit, we define the conjunction in terms of latitude, with the assumption that the proton precipitation bands extend eastward into the LAE emissivity crescent. Specifically, we first compare the MLT-averaged TWINS flux (converted from ENAs to ions; see below) with the latitude-averaged NOAA proton flux (at  $90^\circ$  pitch angle), for a narrow range of magnetic latitude common to both TWINS and NOAA. We also perform a second comparison that includes NOAA data from a wider range of latitude to account for the large uncertainty in TWINS-determined LAE latitude.

#### 4.2.1. Conjunction With Precipitation Band B

[56] For the TWINS MLT-averaged differential ion flux, the sample region includes all pixels (of either TWINS 1 or 2) for which the 50 keV channel flux is at least 30% of the peak value at 50 keV. Note that in our characterization of the MLT extent of the LAE in Figure 4, we included all points above 20% of the peak, in order to capture the majority of the region included in the LAE emissivity crescent. Here we use the slightly higher value of 30% because we wish to minimize the longitudinal roll-off at the edges of the emissivity crescent. Thus defined, the TWINS 1 and 2 sample regions are indicated in Figure 5 by the gray boxes. In MLT, the sampled region is broad: 2034–0236 MLT (TWINS 1) and 1943–0032 MLT (TWINS 2). In magnetic latitude, the sampled pixels span  $67^\circ$ – $74^\circ$  (TWINS 1) and  $70^\circ$ – $74^\circ$  (TWINS 2). We calculated the mean value of

TWINS ENA flux for each of the TWINS 1 and 2 sampled pixel regions. These sample-averaged values are indicated for the 50 keV energy bin by the respective horizontal bars labeled “AVG 1” and “AVG 2” in Figure 5b. The 50 keV TWINS 1 and 2 sample-averaged ENA fluxes are also plotted Figure 6b by the yellow line segments labeled “ENAs.” The horizontal width of the line segments indicates the range of latitude sampled for each quantity. The TWINS 1 and 2 sampled magnetic latitude ranges correspond more closely with the more westward and poleward NOAA precipitation band B.

[57] We converted the TWINS 1 and 2 ENA fluxes to ion fluxes as follows. First, we applied the geometric correction of section 2.2, assuming  $b_h = 300$  km. This correction was applied for all TWINS energy bins; the corrected ENA fluxes at 50 keV are plotted as the line segments labeled “corr” in Figure 6b. The corrected ENA fluxes in all energy bins were then scaled up to ion fluxes using equation (15); the 50 keV values are labeled “Ions” in Figure 6b. These 50 keV (i.e., 25–75 keV) TWINS sample-averaged ion fluxes are in reasonable agreement with those of the 30–80 keV protons measured by NOAA (blue curve) in this same latitude range.

[58] In the next section we compute a single ion spectrum from TWINS and NOAA data, spanning 0.5–800 keV.

#### 4.2.2. TWINS and NOAA Ion Spectrum (B)

[59] TWINS 1 and 2 averaged ion spectral intensities were computed for the 1–50 keV energy bins as follows. At each energy and for each imager, the ENA background level was estimated as the minimum value of ENA flux value from all the pixels along the limb (i.e., not just in the sampled regions indicated by the gray boxes in Figure 5). Note that (as can be seen by inspection of Figure 5) the background ENA level is approximately 10% of the peak signal. The rationale for this subtraction is that from examination of each image, the minimum value along the limb is representative of an ENA signal level that is not localized to the limb and thus is very likely not an LAE signal. The energy- and imager-dependent ENA background was converted to a background ion flux value by applying the geometric correction and TTA analysis. This background level was subtracted from the sample-averaged ion flux at each energy, and for each imager. Finally, at each energy, we took the mean of the TWINS 1 and 2 fluxes.

[60] The NOAA ion spectral intensities were averaged over the TWINS sample latitude range ( $67^\circ$ – $74^\circ$ ), which includes precipitation band B. No background subtraction was performed for the NOAA fluxes because unlike imaging measurements (for which it was verified that the minimum flux value along the limb was representative of the overall background for the image), there is no guarantee that the minimum NOAA proton flux represents the correct background for the selected magnetic latitude interval. Moreover, the minimum NOAA proton flux during 1130–1146 UT is 2 orders of magnitude smaller than the peak value during this interval, so subtraction of this value would be a negligible correction.

[61] The resulting TWINS-NOAA ion spectrum is shown in Figure 7. The cyan-colored curve gives the NOAA-determined portion of the spectrum, spanning 30–800 keV. The solid yellow curve gives the TWINS 1 and 2 averaged

spectral intensity, spanning 0.5–75 keV. The horizontal bars show the energy bins for TWINS and NOAA; the dots are plotted at the linear midpoints of their respective energy bins. The vertical bars on the NOAA points give the standard deviation from the mean (i.e., the average value in the  $67^\circ$ – $74^\circ$  magnetic latitude range). The vertical bar on each TWINS point contains contributions from two sources. The first is the TWINS ENA Poisson counting error (20%, as discussed for Figure 4). The second contribution is the standard deviation from the sample-averaged and imager-averaged mean. That is, each TWINS point is averaged over all sample pixels, and averaged between both imagers. These two contributions (counting error and standard deviation from the mean) are added in quadrature to produce the TWINS vertical error bars. For reference, the dotted yellow curve shows the original ENA fluxes versus energy.

[62] The TWINS spectral shape of Figure 7 is notably different than that found by *Bazell et al.* [2010] for LAE-derived ions during a weakly disturbed interval ( $Dst \sim -30$  nT) on 11 October 2008. For this weak event, TWINS observed monotonically falling ion spectra that roughly follow an  $E^{-1}$  dependence. Similarly monotonically falling spectra were observed in a proton arc by the Poleward Leap sounding rocket on 11 November 1983, during an interval for which  $Dst \sim -40$  nT [*Sørvaas and Aarsnes*, 1996]. In contrast to the monotonic spectra of these weaker events, our spectrum from more strongly disturbed conditions ( $Dst \sim -70$  nT) has a local peak at 4 keV. This difference is attributed to the fact that stronger disturbances ought to produce more peaked ion spectra. Indeed, the peaked 6 April 2010 spectrum is qualitatively consistent with prior TWINS LAE observations during stronger events. *McComas et al.* [2012] measured ENA peak-to-average flux ratios with broad local maxima in the range  $\sim 16$ – $96$  keV, subsequent to the arrival of a solar wind shock on 5 April 2010 (1 day prior to our event interval). *Valek et al.* [2010] reported LAE spectra with broad peaks covering the range  $\sim 2$ – $32$  keV while  $Dst$  varied between  $-25$  nT and  $-66$  nT during a CIR-driven storm on 22 July 2009.

[63] As will be shown in the next section, the local peak in the plot of Figure 7 is the sample-averaged, imager-averaged signature of what is actually a pronounced MLT dependence. Above 50 keV, the NOAA intensity falls very steeply with energy.

[64] Within the ranges of their respective error bars, there is good agreement between the TWINS flux at 50 keV (i.e., the 25–75 keV bin) and the NOAA flux in the 30–80 keV bin. However, five major assumptions are made to obtain this agreement.

[65] 1. First, our geometric correction assumes a LAE vertical (versus altitude) scale size  $b_h = 300$  km. If we choose instead  $b_h = 800$  km, the maximum vertical-scale size estimated based on Figure 1, we obtain the green dashed curve of Figure 7, which is a factor of  $\approx 3$  smaller than the yellow TWINS ion curve. To the degree that the LAE scale size is bounded by  $b_h = 300$ – $800$  km, the green dashed and yellow solid curves represent bounding limits to the TWINS ion spectral intensity’s dependence on  $b_h$ .

[66] 2. The second assumption we make is to neglect MLT dependence of the NOAA proton precipitation bands by assuming these bands, which were actually observed

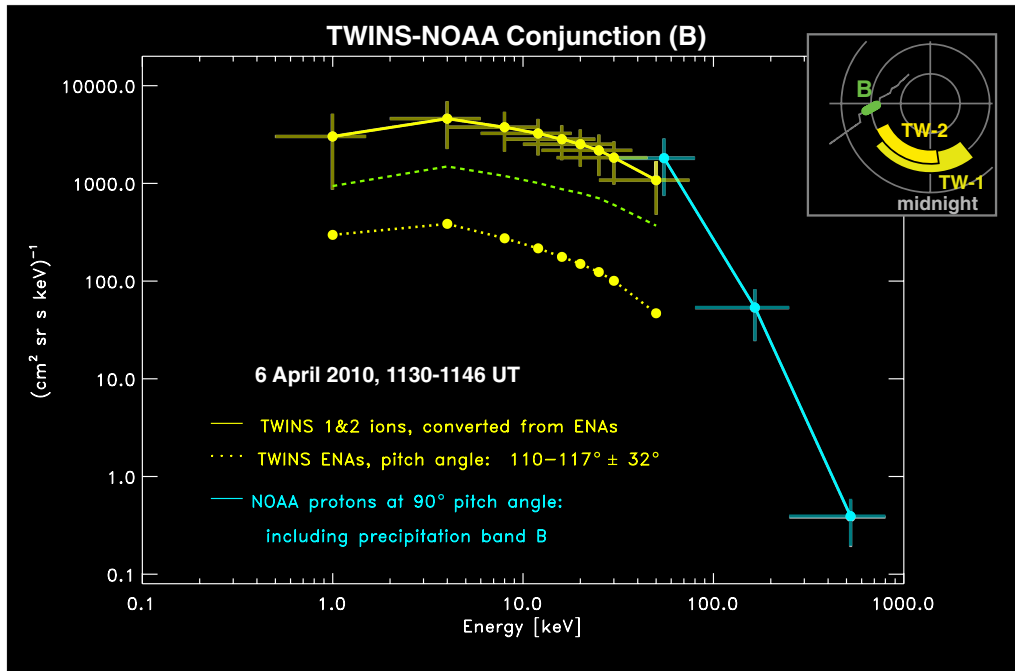


**Figure 7.** Combined TWINS-NOAA ion spectrum, 1130–146 UT on 6 April 2010 from conjunction between TWINS LAEs and NOAA precipitation band B. NOAA protons (cyan curve) at each energy band are averaged over  $67^{\circ}$ – $74^{\circ}$  latitude (i.e., band B). TWINS ions (solid yellow curve) in each energy bin are averaged over all selected pixels and averaged between the two imagers; all intensities have been background subtracted and derived from ENA intensities as described in the text. Also plotted are unmodified TWINS ENAs (yellow dotted line), and ion intensity using alternate geometric correction (green dashed line); see text. The polar dial plot at the top right illustrates the TWINS-NOAA (band B) conjunction.

westward of the main LAE emissivity crescents of both TWINS 1 and 2, extend into the emissivity crescent.

[67] 3. Third, we ignore the substantial uncertainty in the magnetic latitude values that were geometrically determined for the TWINS pixels. Relevant to this latter assumption, averaging the NOAA data over a wider range of latitude, and thus including the factor of 10 stronger, lower-latitude proton precipitation band (Figure 6) produces much higher NOAA spectral intensity, decreasing the level of agreement (cf. next section).

[68] 4. Fourth, we assume that the TWINS pixels included in the sample (and averaged) contain fluxes unmodulated (in either space or energy) by the emissivity function.

[69] 5. Fifth, we assume that it is meaningful to compare the protons observed by NOAA at 850 km altitude with the ion fluxes derived from TWINS LAEs at an unknown but assumed altitude of 400 km. Though we list this assumption for completeness, it is not much of a concern because it is probable that very few downward going ions are lost above 400 km.

[70] Given these multiple assumptions and their associated uncertainties, the agreement between the TWINS and NOAA curves of Figure 7 must be accepted with some caution. Nonetheless, within the constraints of our simplified analysis, Figure 7 does provide limited validation of the conversion of TWINS low-altitude ENA emissions to ion fluxes that can complement both the spatial coverage and energy range of in situ measurements.

#### 4.2.3. TWINS and NOAA Ion Spectrum (A + B)

[71] In Figure 6b, the magnetic latitude range of the selected TWINS pixels very closely matches that of NOAA-observed precipitation band B, and in the previous section, this conjunction yielded fairly good agreement where the energy ranges of the TWINS and NOAA spectra overlap. However, we must acknowledge that the geometrically determined latitudes of TWINS pixels bear a considerable uncertainty, tens of degrees on average (cf. Figure 4). To account for this uncertainty, we calculated a TWINS-NOAA combined ion spectrum for a second definition of conjunction which includes NOAA proton data from a wider range of latitude, i.e., including both NOAA precipitation bands (A and B). The NOAA spectral intensities were computed as an average flux (in each NOAA energy bin) over the magnetic latitude range  $58^{\circ}$ – $74^{\circ}$ , with no background subtraction. The TWINS intensities were computed as described above, including geometric correction, conversion to ions, and background subtraction. The result is shown in Figure 8. The TWINS ion spectrum was multiplied by a factor of 20 to bring it into agreement with the NOAA spectrum. Given the poor level of agreement with the NOAA spectrum in this second conjunction, it is clear that the latitudinal uncertainty of TWINS limb pixels is an impediment to validating the absolute ion fluxes using data from the polar-orbiting NOAA spacecraft. Because TWINS pixels do not resolve the precipitation region, it is not possible to determine a priori which of

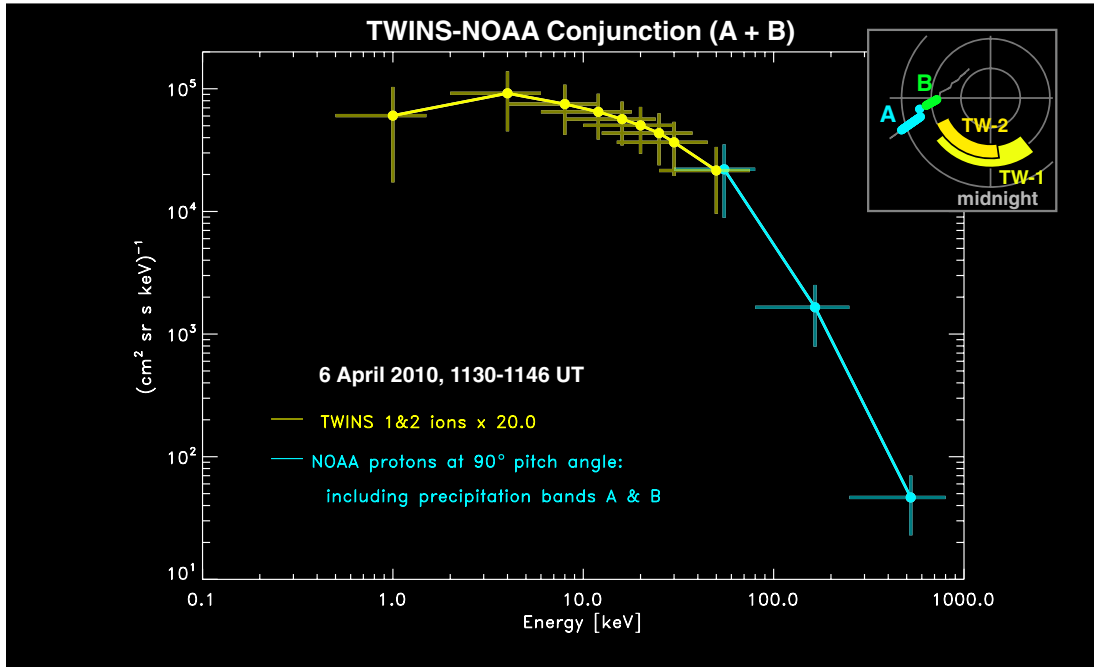


**Figure 8.** Combined TWINS-NOAA ion spectrum, 1130–146 UT on 6 April 2010 from conjunction between TWINS LAEs and both A and B precipitation bands observed by NOAA. To obtain agreement between NOAA 30–80 keV and TWINS 50±25 keV intensities, the TWINS spectrum is multiplied by a factor of 20. The polar dial plot at the top right illustrates the TWINS-NOAA (bands A and B) conjunction.

the NOAA-observed precipitation bands (A, B, or both) contributes to the ENA signal in corresponding TWINS pixels. The MLT separation between the NOAA orbit and the TWINS-observed LAE crescent compounds this difficulty. We conclude, as did *Bazell et al.* [2010], that the shapes of the TWINS-derived ion spectra are more trustworthy than the absolute ion fluxes. This is a nontrivial result because the conversion to ion differential flux using equation (15) involves multiplying ENA spectra by a function of  $\sigma_c$  and  $\sigma_s$  (the energy-dependent charge exchange and stripping cross sections).

## 5. TWINS Individual Pixel Spectra

[72] In the previous section, we performed a comparison between NOAA in situ data and TWINS LAE-derived ion flux, averaged over a broad range of MLT. In this section, we demonstrate that the individual pixel-to-pixel variation in LAEs resolves MLT-dependent low-altitude ion spectral shape information.

[73] Figure 9 shows background-subtracted ion spectra for TWINS 1 (left column) and TWINS 2 (right column). Each curve is obtained from a single pixel selected at or just inside the limb as described in section 2.1.4. The ENA fluxes are converted to ion fluxes and background subtracted as in the previous section, except no averaging of multiple pixels is performed. The individual pixel curves are color coded by MLT (Figures 9a and 9b) or magnetic latitude (Figures 9c and 9d). The same color coding is used for TWINS 1 and 2 in each row.

### 5.1. MLT Dependence

[74] The TWINS ion spectra reveal a pronounced dependence on magnetic local time (Figures 9a and 9b):

[75] 1. East of midnight (cyan and blue curves), the spectra rise slightly from a local minimum at 1 keV to a peak at 4 keV and then fall steeply and monotonically with energy above 4 keV.

[76] 2. West of about 2200 MLT (orange and red curves), the spectral shapes are quite different from those of post-midnight: there are dips in relative (to the peak) intensity at the lowest energy, and these low-energy dips become more pronounced as one moves westward. With decreasing (i.e., more westward) MLT, the spectra become increasingly flattened between  $\sim 4$  and 30 keV, producing a broad peak that shifts to higher energies with decreasing MLT. At the most westward locations, there emerges a thermal-like peak above 10 keV. For comparison, a 12.3-keV thermal spectrum ( $J_0 E \exp[-E/kT]$ ) is plotted over the most duskward spectra for TWINS 1 and 2. The TWINS 2 spectrum at 1943 MLT (Figure 9b, red curve) agrees quite well with the 12.3 keV thermal spectrum above 8 keV.

[77] 3. At intermediate MLT locations (green and yellow curves), the spectral shapes exhibit a transition between those of the pre-2200 MLT and postmidnight sectors. Although these spectra do not exhibit a clear thermal-like peak, they certainly do not fall as steeply (in the range 4–50 keV) as the postmidnight spectra. The general trend is a shift toward more energetic, more peaked spectra with decreasing (more westward) MLT.

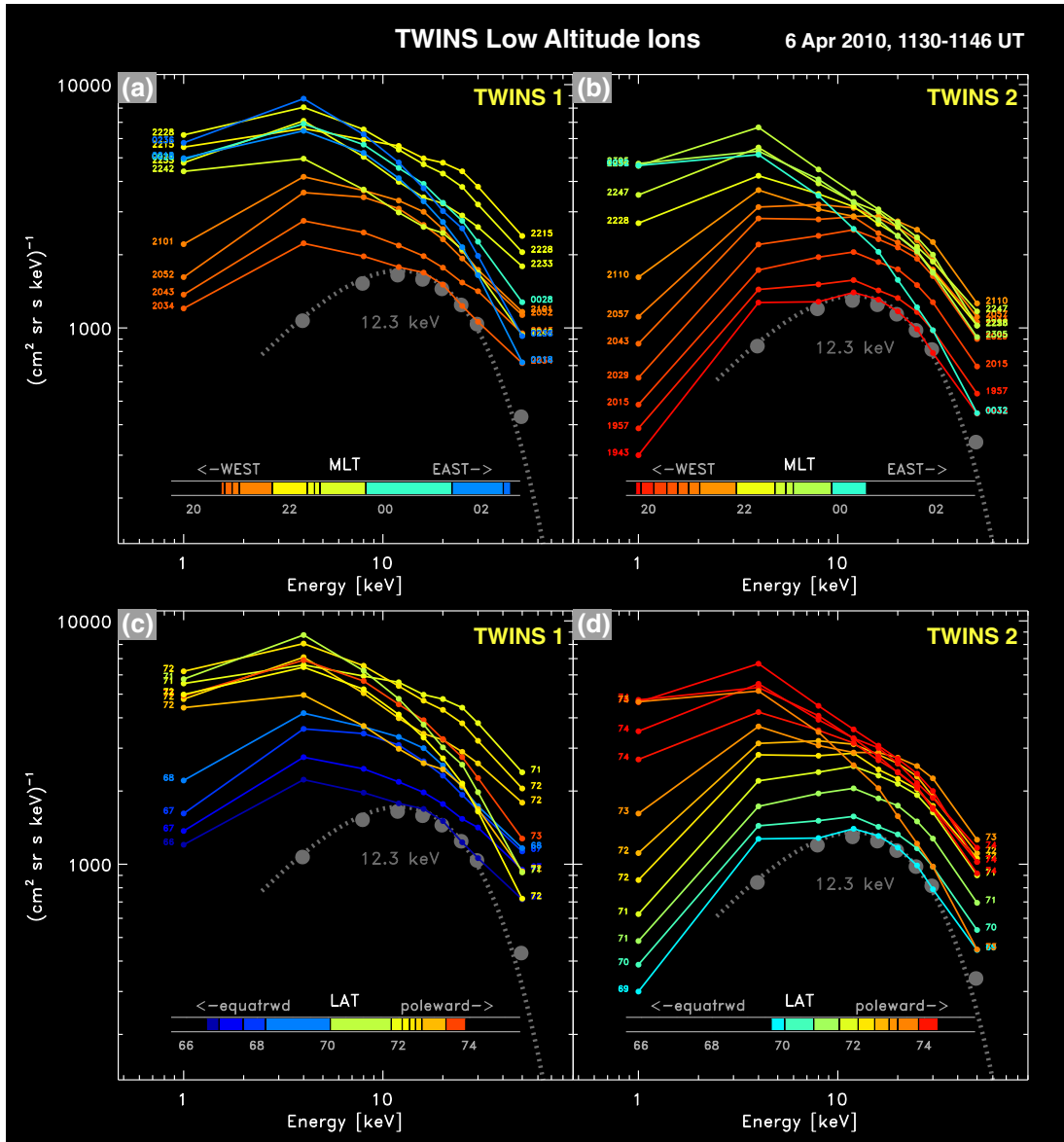


**Figure 9.** Background-subtracted ion spectra for TWINS 1 (left column) and TWINS 2 (right column), 1130–146 UT on 6 April 2010. Each curve is obtained from a single limb pixel as described in the text. The individual-pixel spectral curves are color coded by (a and b) MLT or (c and d) latitude. The same color coding is used for TWINS 1 and 2 in each row. The dotted gray curve is a thermal spectrum at 12.3 keV. The gray dots indicate the effect of energy binning: each dot is at point  $(E_j, M_j)$ , where  $E_j$  is the center value of each TWINS energy bin, and  $M_j$  is the average value of the Maxwellian function over each energy bin. There is negligible effect of energy binning except for the 50 keV bin.

[78] This trend is consistent with ion drift physics: lower energy ions act under the influence of both an eastward  $E \times B$  drift and a westward magnetic gradient-curvature drift, whereas higher-energy ion drifts are dominated by westward magnetic drift. More energetic ions will (on average) migrate westward under the influence of gradient-curvature drift, and the least energetic ions will tend to drift eastward under the influence of the magnetospheric electric field. Comparison of the two sets of spectra from TWINS 1 and 2 also shows reasonable consistency in terms of absolute MLT, i.e., curves with similar MLT in the left and right panels tend to have

similar spectral shapes. Said another way, one could combine the TWINS 1 and 2 spectra into a single group and obtain the trend toward more energetic spectra for more westward locations.

[79] We compare the MLT dependence of the TWINS individual pixel ion spectra of 6 April 2010 with two prior results:

[80] 1. *Bazell et al.* [2010] derived ion spectra from TWINS LAEs during a very weak geomagnetic disturbance (11 October 2008) with  $Dst \sim -30$  nT and  $Kp = 3.3$  and found a similar MLT dependence to our study: more energetic spectra at more westward MLT. They sampled two

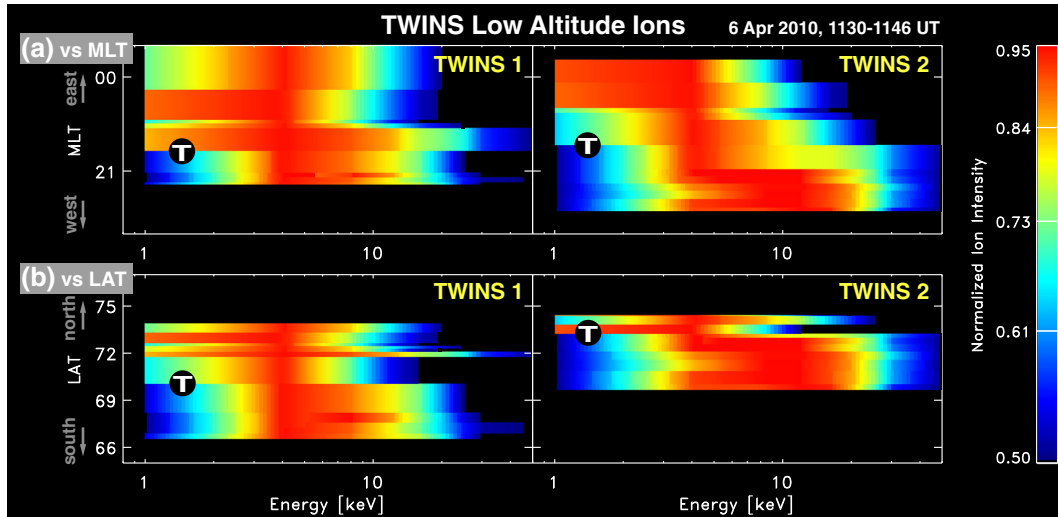


**Figure 10.** Normalized 2-D spectra for TWINS 1 (left column) and TWINS 2 (right column), plotted versus (a) MLT and energy and (b) latitude and energy. Each row of 2-D spectrum plots the 100-point-interpolated (see text) intensity versus energy, normalized to its peak intensity at that MLT or latitude.

MLT locations, 0450–0500 MLT and 2200 MLT. The more eastward spectra (0450–0500 MLT) decreased by a factor of 10 between 1–40 keV, whereas the more westward spectrum (2200 MLT) decreased by a factor of 3–4 in the same energy range. However, their spectra contained neither the low-energy dip observed on 6 April 2010, nor the thermal-like peak above 10 keV. These results are not inconsistent because the 6 April 2010 spectra were obtained during a more disturbed period ( $Dst \sim -70$  nT,  $Kp = 4.7$ ) than those of 11 October 2008, during which it might be expected to see a shift toward slightly higher energies (and thus a relative dip at 1 keV and a peak at 4 keV).

[81] 2. Hardy *et al.* [1989] analyzed 26.5 million 1 s spectra in the 30 eV to 30 keV range, obtained by the DMSP F6 and F7 spacecraft. They calculated average spectra, binned in MLT and  $Kp$ . Their average spectra for  $Kp = 5$  (i.e., similar to the conditions on 6 April 2010) did not contain local low-energy peaks in the 1–50 keV TWINS energy range, but did show significantly more energetic spectra at midnight than at dawn, consistent with the 6 April TWINS spectra. Their midnight and dusk spectra also contain evidence of 10–20 keV thermal spectral peaks qualitatively similar to the 12.3 keV peak that on 6 April 2010 TWINS observed in the same MLT range.

## 5.2. Latitude Dependence

[82] Figures 9c and 9d show the latitudinal dependence. For each imager’s set of spectral curves (TWINS 1 or 2), the more peaked, energetic spectra are found at lower magnetic latitudes. Unlike for the MLT dependence, though, comparison of the two sets of spectra from TWINS 1 and 2 does not show consistency in terms of absolute latitude. For example, the 69° (cyan) curve of TWINS 2 has a more energetic, more peaked spectral shape than the 66° (blue) curve of TWINS 1, in contradiction of the single-imager trend toward more energetic spectra at more equatorward latitude. This lack of consistency between the absolute latitudinal dependencies of the two imagers reflects the significant uncertainty in the latitude determination. This absolute-latitude mismatch

could also be a real effect of more localized variations. However, the fact that the mismatch occurs for an MLT range simultaneously sampled by both imagers is evidence against this explanation. In terms of relative latitude, however, the trend toward more energetic spectra at lower latitudes is also consistent with drift physics. For a given energy, the ion drift trajectory is at lower  $L$  (and lower latitude) near dusk than dawn. Thus, the latitudinal dependence of the TWINS ion spectra seems to be a byproduct of the strong MLT dependence: given the trend toward more energetic ions near dusk than dawn, then it will also be the case that the more energetic ions will follow drift trajectories closer to the Earth (i.e., lower latitude).

## 5.3. Normalized Spectra

[83] To illustrate further the MLT and latitudinal dependencies just discussed, Figure 10 shows normalized 2-D spectra for TWINS 1 (left column) and TWINS 2 (right column), plotted versus MLT and energy (top row) and magnetic latitude and energy (bottom row). Each row of a 2-D spectrum plots the spectral intensity versus energy, normalized to its peak value at that MLT or latitude. Each TWINS limb pixel’s nine-point energy bin-sampled spectrum has been linearly interpolated to a 100-point, logarithmically spaced energy array spanning 1–50 keV. The rationale for doing this is to facilitate comparison with the line-plot spectra of Figure 9, with the assumption that in the line plots, the visual shape of the spectra is more easily perceived via the line segments (each of which is a linear interpolation) linking individual points. As with Figure 9, the 2-D spectra of Figure 10 show a clear trend toward spectra with peaks at higher energy for more westward MLT locations. There is a less clear/consistent trend toward peaks at higher energy for more equatorward latitudes. The reasonable consistency in absolute MLT between TWINS 1 and 2 is illustrated by the fact that the transition (labeled “T”) to spectral shapes with a sharp dip in intensity at the lowest energy (i.e., the blue pixels at the lowest energies) occurs at about the same MLT in both plots: at approximately 2140 MLT in Figure 10a and

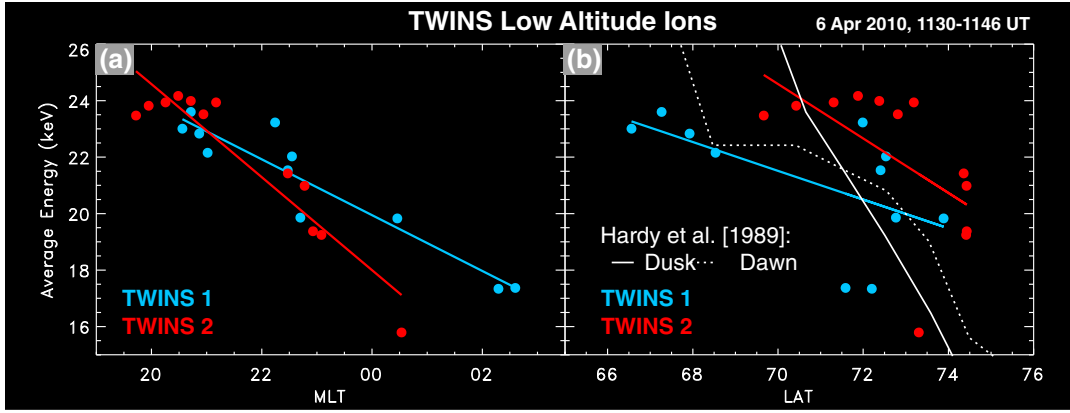


**Figure 11.** Average energy  $E_{AVE}$ , plotted for TWINS 1 and 2, versus (a) MLT and (b) latitude. Solid red and blue lines are linear fits (see text for fit parameters). White curves in versus latitude plot are re-normalized  $E_{AVE}$  curves from dawn (dotted line) and dusk (solid line), adapted from *Hardy et al.* [1989], as described in the text.

2150 MLT in Figure 10b. The lack of consistency in absolute latitude is similarly illustrated by the different (for TWINS 1 versus TWINS 2) latitudinal locations of this transition (T): at approximately  $70^\circ$  in Figure 10c and  $73^\circ$  in Figure 10d.

#### 5.4. Average Energy

[84] Following *Hardy et al.* [1989], the spectra of Figure 9 were used to calculate the average ion energy at each TWINS limb pixel:

$$E_{AVE} = \frac{\text{integral energy flux}}{\text{integral number flux}} = \frac{\sum J_i E_i \Delta E_i}{\sum J_i \Delta E_i} \quad (21)$$

where quantities are summed from  $i = 0 \dots 8$  corresponding to the nine TWINS energy bins,  $J_i$  is the ion differential flux for each TWINS energy bin,  $\Delta E_i$  is the width of the energy bin, and  $E_i$  is the value of energy at the center of each bin.

[85] In Figure 11, the average energy  $E_{AVE}$  is plotted for TWINS 1 and 2, versus MLT and magnetic latitude. Also plotted are linear fits for each imager's  $E_{AVE}$  data, given by

MLT Fit :	Latitude( $\Lambda$ ) Fit :	
<b>TWINS 1:</b> $23.9 - 1.0(\text{MLT} - 20)$	$23.6 - 0.5(\Lambda - 66^\circ)$	(22)
<b>TWINS 2:</b> $24.6 - 1.6(\text{MLT} - 20)$	$28.5 - 1.0(\Lambda - 66^\circ)$	

In Figure 11a the TWINS 1 and 2 MLT fits are similar, with slopes differing by 37.5% and MLT = 2000 intercepts differing by 3%, providing additional evidence for consistency of the spectral dependence on absolute MLT. In Figure 11b, the TWINS 1 and 2 latitude fits are less similar (slopes differing by 50%,  $\Lambda = 66^\circ$  intercepts differing by 17%), consistent with a less certain absolute latitude determination.

[86] The calculated values of  $E_{AVE}$  provide a quantitative measure of the already-discussed trends favoring more peaked, more energetic spectra at more westward MLT and at more equatorward latitude. The physical interpretation of the  $E_{AVE}$  curves is the same as that of the individual pixel spectra. The average ion energy is greater near dusk and at lower latitude, consistent with ions of different energies acting under the influence of both the magnetospheric convection electric field and the magnetic gradient-curvature drift.

[87] *Hardy et al.* [1989] plotted dawn and dusk values of  $E_{AVE}$  versus dipole  $L^{-2}$ , for  $Kp = 5$ , i.e., the  $Kp$  level

of our 6 April 2010 event. (In the case of the dawn curve, they plotted normalized  $E_{AVE}$ .) Qualitatively consistent with our plot Figure 11b, they found duskside  $E_{AVE}$  increased with decreasing latitude. More quantitatively, *Hardy et al.* found a linear relationship for  $E_{AVE}$  versus dipole  $L^{-2}$  near dusk, indicating  $E_{AVE}$  values consistent with adiabatic compression. Near dawn, they found a linear relationship above  $\Lambda \approx 70^\circ$ . Using a cursor-based Interactive Data Language algorithm, we extracted normalized  $E_{AVE}$  versus  $L^{-2}$  data from scanned versions of their Figures 15 (duskside curve) and 17 (dawnside). We converted the  $L^{-2}$  values to  $\Lambda$  using a dipole field. To compare these normalized  $E_{AVE}$  versus  $\Lambda$  curves with our Figure 11b, we re-normalized the *Hardy et al.* curves to be 22 keV (the mean  $E_{AVE}$  value of both TWINS 1 and 2 fits) at  $72^\circ$  (the mean latitude of both fits). These two re-normalized curves, plotted as the solid (Dusk) and dotted (Dawn) lines, follow the general trend of the TWINS 1 and 2  $E_{AVE}$  versus  $\Lambda$  data. Therefore, within the limits of the considerable uncertainty in TWINS pixel latitude, the TWINS precipitating ion spectra agree with the results of *Hardy et al.* [1989] and are thus not inconsistent with adiabatic compression. The existence of any consistency whatsoever in the latitudinal dependence is evidence that relative magnetic latitude of TWINS limb pixels is not meaningless despite the large uncertainty in absolute latitude value.

#### 5.5. MLT Scale Size Resolved by TWINS

[88] As mentioned in section 2.1.5, the TWINS imagers are each mounted on a rotating actuator that sweeps back and forth over an approximately Earth-centered viewing cone. Each imager has an instantaneous field of view (FOV) of  $140^\circ$ -by- $4^\circ$ , with the second dimension being the slit-camera width [*McComas et al.*, 2009a, 2012; *Valek et al.*, 2010]. In skymap-projected images (e.g., Figure 4), the sky is discretized into  $4^\circ$ -by- $4^\circ$  pixels in both imaging angle ( $\lambda$ ) and azimuthal (actuation) angle ( $\beta$ ). Because near the center of the skymap-projected image the imager's slit-camera width is larger than the azimuthal size  $\delta\beta$  of the wedge-shaped pixels, each LAE pixel contains counts from a wider range of  $\beta$  than the boundaries of the pixel. As occurs for any such boxcar averaging, this leads to smearing in MLT,

because the actuation angle  $\beta$  most closely corresponds to the geophysical MLT coordinate. Therefore, although there is a clear and pronounced MLT dependence found in the TWINS spectra of Figure 9 and their derived values of  $E_{AVE}$  in Figure 11, it is also true that there is a finer-scale MLT dependence that cannot be resolved by TWINS because of the finite-width slit camera. Assuming an LAE located on the limb ( $r = a$ ) directly opposite from the TWINS imager, we estimate the minimum scale size for MLT structure that can be resolved by the  $4^\circ$ -wide slit-camera to be

$$\delta S_{MLT} = \frac{1}{2} (12h) \frac{4^\circ}{2 \omega_{limb}}, \quad (23)$$

an estimate obtained by calculating the fraction of the limb ( $2 \omega_{limb}$  angular size, or 12 MLT h wide) subtended by the  $4^\circ$  angular width of the slit-camera. From a vantage point approximately  $6 R_E$  away, this estimate yields  $\delta S_{MLT} \sim 1$  MLT h. Thus, although our knowledge of the MLT location of the center of a TWINS LAE pixel is uncertain to within  $\pm \delta MLT_a \approx \pm 0.5$  h (section 2.1.5), the TWINS imager's finite slit-camera width smears out structures smaller than about  $2 \delta MLT_a$ . This smearing is evident in the spectra of Figures 9 and 10. Line spectra from adjacent (in MLT) pixels are very similar to each other, and the normalized 2-D spectra show evidence of  $\sim 1$  h wide "banding" in local time. Also consistent with the estimated  $\delta S_{MLT}$  above, in the TWINS 1 ENA flux versus MLT plot of Figure 4b, the narrower peak in the two-component Gaussian fit has an MLT half-width of  $W_{MLT} = 0.9$  h (section 3.1.1). Note that in terms of instrument angular response, the  $4^\circ$  slit-camera width corresponds to the full-width half-maximum of the counts versus non-imaging angle calibration curve [McComas *et al.*, 2009a, Figure 41b]. Including count rates below the half-maximum value would double the estimate given in equation (23).

### 5.6. Effect of Statistical Smoothing

[89] A standard part of the TWINS image-making process includes an algorithm called "statistical smoothing" [McComas *et al.*, 2009b; Valek *et al.*, 2010; McComas *et al.*, 2012]. This algorithm adaptively assigns pixel counts to obtain a desired level of minimum statistical certainty, for the entire image. For this study, we require 25 counts per pixel (i.e.,  $\leq 20\%$  Poisson statistics) throughout the image. It is worth emphasizing the adaptive nature of statistical smoothing; regions of the original image that already have 25 counts are unaffected by the algorithm.

[90] It is natural to wonder whether statistical smoothing may influence the results and conclusions presented in this paper. It is known that the LAE is a very localized feature, and thus in principle two adjacent pixels may have very different ENA fluxes. However, because LAEs are generally the brightest feature of a TWINS image, and thus already have more than 25 counts per pixel, LAEs are generally unaffected by the smoothing algorithm. We checked the effects of statistical smoothing on our results by running our analysis both with and without statistical smoothing. There are no significant differences between these two versions of our analysis:

[91] 1. The plots of ENA flux within the high-flux LAE region (sections 3.1–3.4) are visually indistinguishable regardless of whether or not smoothing is applied.

[92] 2. Spectra from fluxes averaged over the entire LAE region (section 4) are likewise the same in both versions of our analysis.

[93] 3. Individual pixel spectra (section 5) are all qualitatively identical and are quantitatively virtually identical in most cases, as follows. Spectra obtained from the brightest part of the LAE (west of about 2200 MLT) are identical in both versions. For energies above about 10 keV, the lower flux spectra from east of 2200 MLT are slightly "noisy" (i.e.,  $\leq 10\%$  fluctuation from the smoothed spectra). Spectral shapes and their interpretation are the same.

[94] 4. Integrated quantities (also section 5) are nearly identical (to within about 20%) for the two versions of our analysis.

[95] 5. Using unsmoothed images, values of the peak half-width at 12 and 16 keV are approximately 50% lower than that of the smoothed images (Appendix A), but only for the assumption that the peak occurs at the dawn limb (blue curve). For the peak-at-dusk assumption (red curve) the half-width curve is unchanged.

[96] In summary, we find no significant difference between the two versions of the analysis (smoothed versus unsmoothed). All of our results are virtually identical in both versions, and our conclusions (section 6) are not affected by whether or not smoothed images are used. For more about the statistical smoothing algorithm, see the detailed discussion in Appendix A2 of McComas *et al.* [2012].

## 6. Summary and Conclusions

[97] In this paper, we have presented observations and analysis of ENAs produced from the low altitude emission (LAE) region during the interval 1130–1146 UT on 6 April 2010. In place of more rigorous numerical calculation of the emissivity function, we implement a simplified version of the thick-target analysis (TTA) of Bazell *et al.* [2010] that includes a geometric correction of the ENA flux. Since the TTA is limited to the brightest portion of LAEs, we apply our analysis for pixels with at least 30% of the peak value. With proper caution in interpreting the results, our simplified approach (with its set of approximations) does yield useful quantitative information about the source ion distribution.

[98] We show that TWINS ENA imaging can resolve MLT-dependent low-altitude ion spectral shape information simultaneously across a broad range of MLT and can discern the relative latitudinal dependence. We find a clear and pronounced local time dependence of the spectral properties of precipitating ions, favoring more energetic ions near dusk than dawn. This result demonstrates the degree to which pixel-by-pixel variation in LAEs can resolve MLT spatial structure, which advances previous results that considered much coarser MLT structure via averages of larger groups of pixels from the LAE region. Although we include a quantitative validation study of the TWINS-derived ion differential flux using simultaneous NOAA 17 data, our conclusions about MLT-dependent precipitating ion energetics are dependent upon the shape of the derived spectra rather than the absolute magnitude.

[99] The broad coverage of local time dependent ion precipitation provided by TWINS imaging can provide useful contextual information for models and local measurements, and/or can complement the spatial and spectral information

from in situ observations. For example, values of average ion energy ( $E_{AVE}$ ) derived from TWINS LAE ion spectra can provide a useful constraint (or metric of performance) for global ring current simulations. Using imaging to derive values of  $E_{AVE}$  across a broad range of MLT augments previous statistical analysis of the local time dependence of ion spectra [Hardy *et al.*, 1989], by providing system level information in a single image rather than in a sequence of temporally decorrelated single-point measurements.

[100] Our specific results and detailed conclusions are summarized in the following four sections.

### 6.1. TWINS LAE Imaging

[101] We present the details of geometrical calculations used to derive the geophysical locations (MLT and magnetic latitude) and local pitch angles of TWINS limb pixels, assuming the LAEs originate from a specified altitude.

[102] We find an analytical solution for limb pixels located within an annular region of the TWINS image bounded above by the specified LAE altitude and below by a minimum angular offset. We estimate the uncertainties in LAE location and pitch angle associated with finite-sized pixels. The pixel-related uncertainty in MLT is approximately 0.5 h. The latitudinal uncertainty is very large (several tens of degrees) for pixels at the limb because imaging lines of sight are tangential to the limb for these pixels. The uncertainty decreases with inward angular offset from the limb. Because TWINS pixels do not resolve the LAE region, there is high uncertainty about where in the latitudinal pixel the real emission occurs. The pitch angle uncertainty is comparable to that of latitude. We estimate the minimum MLT scale size (1 MLT h) that can be resolved because of boxcar-average-type smearing in the image by the finite width of the TWINS slit-cameras. In section A, we compare the observed LAE flux-peak width to expected values for the magnitude of angular scattering in the instrument foils and conclude that (within the limitations of finite pixel size and instrument design) the TWINS-measured LAE flux reflects the MLT distribution of the geophysical source.

### 6.2. Geophysical Distribution of ENAs

[103] We apply our geometrical analysis to study the geophysical distribution of ENA emissions from a 15 min interval of strong LAEs: 1130–1146 UT on 6 April 2010.

[104] For this interval there was a broad (8.4–9.2 h wide) distribution of LAEs in MLT, located on the opposing limb from the two TWINS imagers. This result is consistent with numerical calculation of the emissivity function by Bazell *et al.* [2010] that predicts optimal LAE viewing in a crescent-shaped region at or inside the limb opposite a TWINS imager. The MLT width of the TWINS 2 distribution was approximately 50 min narrower than that of TWINS 1, implying a possible (though highly uncertain) boundary in ion precipitation near the dusk terminator. LAEs were detected by TWINS in the magnetic latitude range 67°–74°, and in a narrow range of pitch angle peaking at 112° for TWINS 1 and 116° for TWINS 2. Though the absolute latitude of an individual pixel cannot be precisely determined, the relative latitude of adjacent pixels does follow a trend that can be used to discern dependence on changes in latitude along the limb.

### 6.3. TWINS-NOAA Validation Study

[105] Through comparison with simultaneous NOAA 17 in situ observations on 6 April 2010, we test the validity of a simplified implementation of the thick-target approximation (TTA) of Bazell *et al.* [2010] to obtain ion spectra from TWINS LAEs.

[106] We circumvent the numerical calculation of the emissivity function and apply a geometry-based correction to ENA differential flux that scales with the ratio of the TWINS pixel size to the smaller angular size of the LAE in the TWINS field of view. For a TWINS imager located 6  $R_E$  from the LAE, the correction factor ranges from 3 to 9 for expected altitudinal thicknesses of the emission region. We develop an analytical fit to the charge exchange and stripping cross sections of Basu *et al.* [1987].

[107] We perform a validation study using a conjunction between the broad (in MLT) region of TWINS-observed LAEs and a simultaneous NOAA-17 polar-orbit pass. NOAA 17 observed two distinct bands of proton precipitation slightly west of the TWINS LAEs: band A (1900–1920 MLT and 58°–66° magnetic latitude) and band B (1805–1825 MLT and 68°–72°). NOAA observed higher fluxes in A, the more eastward and equatorward band. The ion fluxes from TWINS (averaged over the entire LAE region and for both imagers) and NOAA are combined to produce low-altitude ion spectra spanning 0.5–800 keV for two NOAA conjunction intervals: including only band B (which most closely corresponds with the TWINS LAE latitude range and including both bands A and B. In the overlapping energy range of TWINS and NOAA, there is good agreement between the TWINS and NOAA absolute spectral intensities for the band B conjunction. There is a factor of 20 disagreement for the combined band A and B conjunction. We conclude that the shapes of the TWINS-derived ion spectra are more trustworthy than the absolute ion fluxes.

### 6.4. Local Time Dependence of Precipitating Ions

[108] We calculate TWINS ion spectra for individual pixels spanning several hours of MLT along the LAE limb to measure the local time dependence of the energetics of precipitating ions.

[109] The TWINS ion spectra from 6 April 2010 reveal a pronounced dependence on magnetic local time. The general trend is a shift toward more energetic, more peaked spectra with decreasing (more westward) MLT. Spectra obtained from east of midnight fall steeply and monotonically with energy above 4 keV, with a slight dip in intensity at 1 keV. With decreasing (more westward) MLT, spectra become increasingly flatter in the 4–30 keV range, with a broad peak that shifts to higher energies with decreasing MLT. At the most westward locations TWINS observed a thermal-like peak just above 10 keV. The 1 keV dip is increasingly pronounced with more westward MLT. The more energetic ion spectra occur for generally lower latitude TWINS pixels. Average ion energy  $E_{AVE}$  calculated from the TWINS ion spectra is generally higher near dusk and at more equatorward latitudes. The MLT and magnetic latitude trends of these ion spectral shapes and average energies are consistent with ions drifting in both the magnetospheric convection electric field and the nonuniform geomagnetic field. More energetic ions tend to travel farther westward

where drift paths come closer in to the Earth, and less energetic ions tend to drift farther eastward where trajectories are farther out from the Earth.

[110] The peaked ion spectra on 6 April 2010 are notably different than the monotonic,  $(\text{Energy})^{-1}$  dependence found for LAE-derived ions by *Bazell et al.* [2010] for a weaker disturbance on 11 October 2008. However, LAE spectral peaks have been reported for stronger events by *McComas et al.* [2012] and *Válek et al.* [2010]. The MLT dependence of 6 April 2010 TWINS ion spectra is consistent with the two-point MLT sampling obtained by *Bazell et al.* [2010] for 11 October 2008, if one takes into account the different strengths of these two events. The TWINS-observed thermal peak above 10 keV is qualitatively similar to thermal peaks observed near midnight and dusk in the statistical analysis of *Hardy et al.* [1989]. Within the limits of the considerable uncertainty in TWINS pixel latitude, the 6 April 2010 observed latitudinal dependence agrees with the statistical analysis of *Hardy et al.* [1989], which showed consistency with adiabatic compression. The latitudinal trend of 6 April 2010 ion spectra is modest evidence that relative magnetic latitude of TWINS limb pixels is meaningful despite the large uncertainty in absolute latitude.

## Appendix A: LAE Peak Width

[111] Energetic neutrals entering the TWINS 1 or 2 imager must pass through a carbon foil used to derive each ENA's entrance angle and velocity [*McComas et al.*, 2009a]. Incident particles are known to undergo angle scattering as they transit a carbon foil, depending on particle incident energy and foil thickness. This appendix considers the degree to which foil scattering plays a role in determining (or obscuring) the MLT dependence of LAE pixels along the limb. Specifically, we estimate the angular width of the LAE signal and compare it with theoretical and experimental determinations of foil scattering.

[112] Figure A1a contains TWINS 1 images from the interval chosen for this paper, 1130–1146 UT on 6 April 2010. Images at 1 keV and 50 keV, the lowest and highest energy bins, are shown to aid in discussing energy-dependence of foil scattering. The images are presented in a skymap projection as in Figure 4, but without dipole field lines and with ENA differential flux plotted in a linear color scale. We measure the angular size of the LAE in the imaging angle direction (i.e., the radial direction in the skymap image) because the TWINS imager's slit-camera geometry limits angular scattering in the azimuthal direction. For reference, the violet line (labeled "Sampled Intensity") is plotted at constant azimuthal angle, passing through the LAE region in each image (1 or 50 keV). The 50 keV LAE occupies a shorter length along the violet sample line than does the 1 keV LAE, and also its peak is shifted more duskward. The question we wish to answer is whether the linear extent of the LAE along this sample line is dominated by foil scattering, or represents an energy dependent MLT distribution of the parent population of precipitating ions.

[113] We sample the ENA flux along the violet sample line, for each of the TWINS energy bins. The resulting ENA flux-versus-instrument angle profiles are plotted in Figure A1b, color coded by energy. The violet sample line crosses the Earth limb ( $1 R_E$ ) in two locations near dusk and

dawn; for reference, these locations are indicated by vertical lines in the ENA flux plot. To test the influence of foil scattering we consider two idealized cases:

[114] 1. A point-source ENA signal located at the dusk limb, i.e., the limb closer to the center of the image. This case assumes high angular scattering by the carbon foil, i.e., that the entire linear extent of the LAE along the sample line is caused by foil scattering.

[115] 2. A point-source ENA signal located at the dawn limb. This case represents a low estimate for foil scattering, as it assumes the LAE source is confined to the  $r = a$  limb, and that any emissions outside the limb are not geophysical and therefore must be foil scattering.

[116] Thus, for each of the ENA differential flux curves of Figure A1b, we overplot the half-width-half-max (HWHM)  $\Psi_{1/2}$  measured with respect to the dusk limb (open circles) or with respect to the dawn limb (filled circles). These  $\Psi_{1/2}$  data are plotted versus scaled energy  $E_S \equiv (m_H/m)E$  in Figure A1c. The red line (with open circles) gives the curve for the peak/source located at the dusk limb, and the blue curve (filled circles) shows the case of the peak/source located at the dawn limb. Lacking knowledge of the species composition for the 6 April 2010 event, we assume  $m = m_H$ .

[117] *Funsten et al.* [1993] analyzed the scattering versus incident energy for particles transiting nominal  $0.5 \mu\text{g cm}^{-2}$  carbon foils. We performed a linear fit to their experimental and theoretical curves and found the following relations for the angular scattering half-width at half maximum (HWHM)  $\Psi$  for hydrogen (H), helium (He) and oxygen (O):

$$\log_{10} \Psi_H = 1.09074 - 1.00983 \log_{10} E \quad (\text{A1})$$

$$\Psi_{\text{He}} = 2.75 \Psi_H \quad (\text{A2})$$

$$\Psi_O = 10.9 \Psi_H. \quad (\text{A3})$$

The  $\Psi_H$  and  $\Psi_O$  curves are overplotted onto Figure A1c. These curves are, for energies above 3 keV, significantly smaller in magnitude and have a much steeper slope than the two 6 April  $\Psi_{1/2}$  curves.

[118] The yellow curve of Figure A1c plots the experimental values of  $\Psi_{1/2}$  determined from laboratory calibration of the TWINS 1 flight instrument. The calibration  $\Psi_{1/2}$  values at lower energies ( $E_S < 10$  keV) are the laboratory-determined values for angular scattering in the foils, and are comparable in magnitude to the *Funsten et al.* curves. At higher energies, calibration values level off to a  $\Psi_{1/2}$  value of  $\sim 3.5^\circ$ , which is not a foil-scattering effect but is rather the intrinsic resolution of the instrument determined by the degree of signal spreading in the instrument MCPs and anode.

[119] The ratios of the blue and red solid curves to the calibration data are plotted as red and blue dashed curves. For both assumptions (peak at dusk vs. dawn limb), the 6 April 2010  $\Psi_{1/2}$  data (except for the 50 keV point on the blue curve) are a factor of 2–5 larger than the calibration data. Since the on-orbit foil scattering is no different than that measured in the laboratory, we interpret the 6 April 2010  $\Psi_{1/2}$  values as evidence that the LAE signal is not a point source, and the extended distribution along the limb cannot be explained entirely (or even mostly) as angular scattering in the carbon foils. That is, we believe the along-the-limb MLT dependence of TWINS-measured LAE flux reflects at least in part the MLT distribution of the geophysical source.

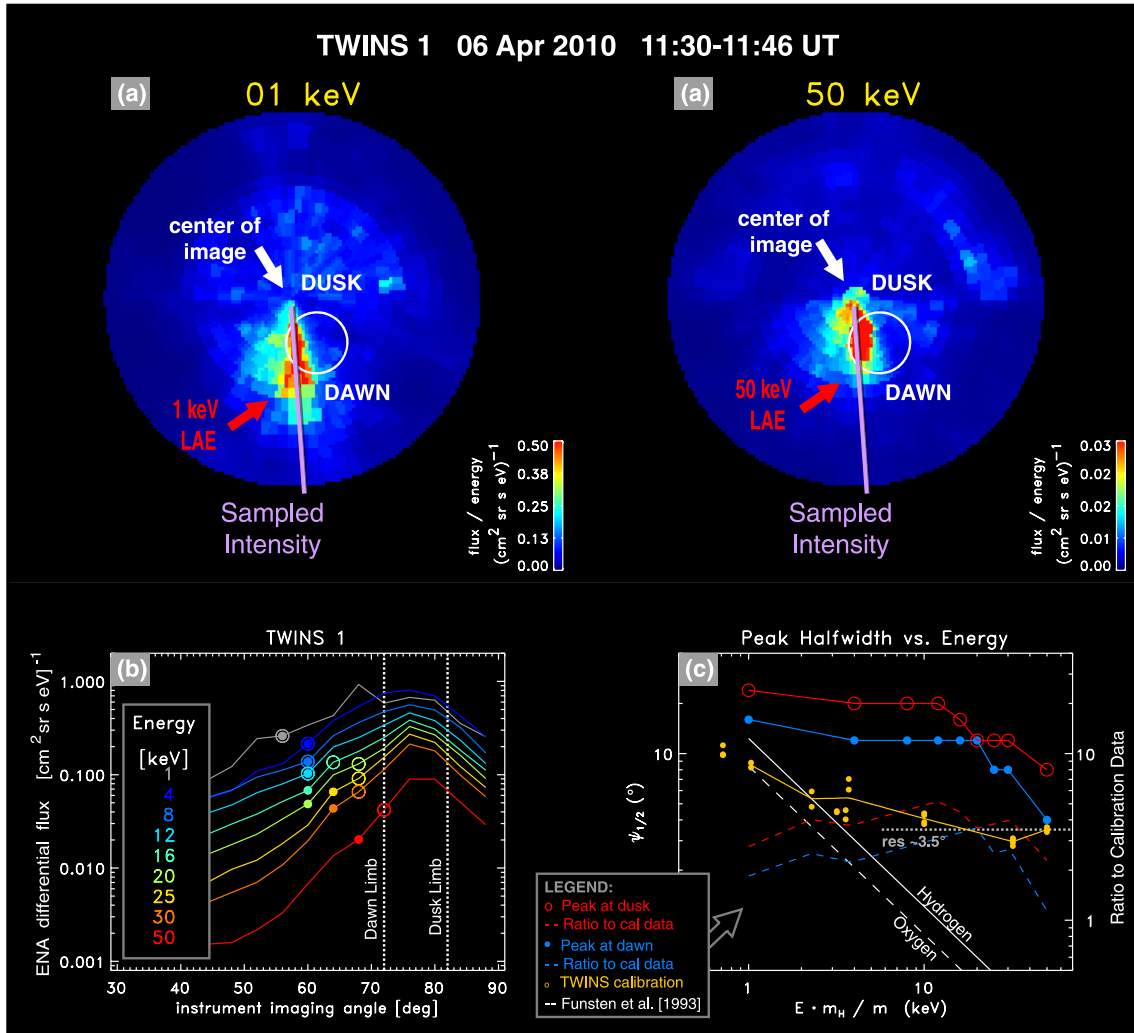


**Figure A1.** Characterization of the width of TWINS-observed LAE signals and comparison with expected values associated with angular scattering in the instrument foils. (a) TWINS 1 images at 1 keV and 50 keV. The circle is the Earth limb ( $r = 1 R_E$ ). At each energy, LAE intensity is sampled along the violet line at constant instrument actuation angle. (b) LAE intensity versus instrument imaging angle along the violet line, for nine TWINS energy bins. Two definitions of peak half-width are indicated by the open circles (assuming the peak at the dusk limb) and filled circles (peak at the dawn limb). (c) Peak half-widths plotted versus mass-scaled energy, compared to published values [Funsten *et al.*, 1993] and TWINS calibration values (yellow curve). The dashed lines are the ratios to the calibration values.

This assertion is bolstered by the geophysically consistent MLT dependence of derived ion spectra, found in Figure 9. Furthermore, inspection of the image at 50 keV (at which energy we expect scattering to be entirely negligible) shows there is a distributed (in MLT) source.

[120] Foil scattering is largest at the lowest energies. According to the TWINS calibration data the HWHM scattering at 1 keV is 8–9°, or 2 pixels. Therefore, we considered whether the reduction in spectral intensity at 1 keV, found in the line spectra of Figure 9, might be caused in part by scattering. It is possible that 8°–9° foil scattering could reduce the 1 keV flux for a given limb pixel, by displacing counts to adjacent or nearby pixels. We tested this hypothesis by calculating spectra that included all possible LAE pixels, including pixels well outside the limb. This test was

performed for two types of pixel selection: manual and automated, i.e., select all pixels with fluxes above a fraction  $f_p$  of the peak. For both manual and automated LAE pixel selection (the latter with various peak fractions  $f_p$ ), the LAE spectra all contained evidence of the 1 keV reduction in spectral intensity, although the magnitude of the “dip” varied slightly (by a few percent). In addition, from examination of the full energy and MLT range of the spectra in Figure 9, it is clear that the intensity reduction at 1 keV is consistent with the rest of the spectra at higher energies, for which foil scattering is smaller than the intrinsic resolution of the instrument. Therefore, we conclude that the general trend of reduced intensity at the lowest energies is a real geophysical effect, and not an artifact of angular scattering in the instrument foils.

[121] **Acknowledgments.** We thank E. C. Roelof for an illuminating discussion of the physics and interpretation of low altitude ENA emissions. This project was supported as a part of the NASA TWINS mission in NASA's Explorer Program. Final and Provisional *Dst* index values were kindly provided by the World Data Center for Geomagnetism, Kyoto University, Japan.

## References

- Bailey, J. J., and M. Gruntman (2011), Experimental study of exospheric hydrogen atom distributions by Lyman-alpha detectors on the TWINS mission, *J. Geophys. Res.*, *116*, A09302, doi:10.1029/2011JA016531.
- Barabash, S., P. C. Brandt, O. Norberg, R. Lundin, E. C. Roelof, C. J. Chase, B. H. Mauk, and H. Koskinen (1997), Energetic neutral atom imaging by the Astrid microsatellite, *Adv. Space Res.*, *20*, 1055, doi:10.1016/S0273-1177(97)00560-7.
- Basu, B., J. R. Jasperse, R. M. Robinson, R. R. Vondrak, and D. S. Evans (1987), Linear transport theory of auroral proton precipitation—A comparison with observations, *J. Geophys. Res.*, *92*, 5920, doi:10.1029/JA092iA06p05920.
- Bazell, D., E. Roelof, T. Sotirelis, P. Brandt, H. Nair, P. Valek, J. Goldstein, and D. McComas (2010), Comparison of TWINS images of low-altitude emission (LAE) of energetic neutral atoms with DMSP precipitating ion fluxes, *J. Geophys. Res.*, *115*, A10204, doi:10.1029/2010JA015436.
- Brandt, P. C., S. Barabash, E. C. Roelof, and C. J. Chase (2001a), Energetic neutral atom imaging at low altitudes from the Swedish microsatellite Astrid: Observations at low ( $\leq 10$  keV) energies, *J. Geophys. Res.*, *106*, 24663, doi:10.1029/2000JA900119.
- Brandt, P. C., S. Barabash, E. C. Roelof, and C. J. Chase (2001b), ENA imaging at low altitudes from the Swedish microsatellite Astrid: Extraction of the equatorial ion distribution, *J. Geophys. Res.*, *106*(A11), 25731.
- Brandt, P. C., P. S. Ohtani, D. G. Mitchell, M.-C. Fok, E. C. Roelof, and R. DeMajistre (2002), Global ENA observations of the storm mainphase ring current: Implications for skewed electric fields in the inner magnetosphere, *Geophys. Res. Lett.*, *29*(20), 1954, doi:10.1029/2002GL015160.
- Brandt, P. C., D. G. Mitchell, E. C. Roelof, S. M. Krimigis, C. P. Paranicas, B. H. Mauk, J. Saur, and R. DeMajistre (2005), ENA imaging: Seeing the invisible, *Johns Hopkins APL Tech. Digest*, *26*(2), 143.
- Brandt, P. C., et al. (2004), IMAGE/HENA: Pressure and current distributions during the 1 October 2002 storm, *Adv. Space Res.*, *33*(5), 719.
- Buzulukova, N., M. C. Fok, J. Goldstein, P. Valek, D. McComas, and P. C. Brandt (2010), Ring current dynamics in modest and strong storms: Comparative analysis of TWINS and IMAGE/HENA data with CRCM, *J. Geophys. Res.*, *115*(A12), A12234, doi:10.1029/2010JA015292.
- Buzulukova, N., M.-C. Fok, E. C. Roelof, J. Redfern, J. Goldstein, P. Valek, and D. J. McComas (2012), Comparative analysis of low altitude ENA emissions in two substorms, *J. Geophys. Res.*, *118*, 724–731, doi:10.1002/jgra.50103.
- Connors, M., C. T. Russell, and V. Angelopoulos (2011), Magnetic flux transfer in the 5 April 2010 Galaxy 15 substorm: An unprecedented observation, *Ann. Geophys.*, *29*, 619, doi:10.5194/angeo-29-619-2011.
- Fok, M. C., N. Buzulukova, S. H. Chen, P. W. Valek, J. Goldstein, and D. J. McComas (2010), Simulation and TWINS observations of the 22 July 2009 storm, *J. Geophys. Res.*, *115*(A12231), A12, doi:10.1029/2010JA015443.
- Funsten, H. O., D. J. McComas, and B. L. Barraclough (1993), Ultrathin foils used for low-energy neutral atom imaging of the terrestrial magnetosphere, *Opt. Eng.*, *32*, 3090.
- Goldstein, J., P. Valek, D. J. McComas, and J. Redfern (2012a), Latitudinal anisotropy in ring current energetic neutral atoms, *Geophys. Res. Lett.*, *39*, L08102, doi:10.1029/2012GL051417.
- Goldstein, J., P. Valek, D. J. McComas, and J. Redfern (2012b), TWINS energetic neutral atom observations of local-time-dependent ring current anisotropy, *J. Geophys. Res.*, *117*, A11213, doi:10.1029/2012JA017804.
- Grimes, E. W., J. D. Perez, J. Goldstein, D. J. McComas, and P. Valek (2010), Global observations of ring current dynamics during CIR-driven geomagnetic storms in 2008, *J. Geophys. Res.*, *115*(A11), A11207, doi:10.1029/2010JA015409.
- Hardy, D. A., M. S. Gussenhoven, and D. Brautigam (1989), A statistical model of auroral ion precipitation, *J. Geophys. Res.*, *94*, 370, doi:10.1029/JA094iA01p00370.
- Henderson, M. G., et al. (1997), First energetic neutral atom images from Polar, *Geophys. Res. Lett.*, *24*, 1167.
- Ilic, R., R. M. Skoug, H. O. Funsten, M. W. Liemohn, J. J. Bailey, and M. Gruntman (2012), The impact of geocoronal density on ring current development, *J. Atmos. Solar-Terr. Phys.*, doi:10.1016/j.jastp.2012.03.010, in press.
- Keese, A., N. Buzulukova, J. Goldstein, D. J. McComas, E. E. Scime, H. Spence, and K. Tallaksen (2011), Remote observations of ion temperatures in the quiet time magnetosphere, *Geophys. Res. Lett.*, *38*, L03104, doi:10.1029/2010GL045987.
- Keese, A. M., J. G. Elfriz, D. J. McComas, and E. E. Scime (2012), Inner magnetosphere convection and magnetotail structure of hot ions imaged by ENA during a HSS-driven storm, *J. Geophys. Res.*, *117*, A00L06, doi:10.1029/2011JA017319.
- Krimigis, S. M., D. G. Mitchell, E. C. Roelof, K. C. Hsieh, and D. J. McComas (2009), Imaging the interaction of the heliosphere with the interstellar medium from Saturn with Cassini, *Science*, *326*, 971, doi:10.1126/science.1181079.
- Mauk, B. H., D. G. Mitchell, S. M. Krimigis, E. C. Roelof, and C. P. Paranicas (2003), Energetic neutral atoms from a trans-Europa gas torus at Jupiter, *Nature*, *421*, 920, doi:10.1038/nature01431.
- McComas, D. J., N. Buzulukova, M. G. Connors, M. A. Dayeh, J. Goldstein, H. O. Funsten, S. Fuselier, N. A. Schwadron, and P. Valek (2012), Two Wide-Angle Imaging Neutral-Atom Spectrometers and Interstellar Boundary Explorer energetic neutral atom imaging of the 5 April 2010 substorm, *J. Geophys. Res.*, *117*, A03225, doi:10.1029/2011JA017273.
- McComas, D. J., et al. (2009a), The two wide-angle imaging neutral-atom spectrometers (TWINS) NASA mission-of-opportunity, *Space Sci. Rev.*, *142*, 157, doi:10.1007/s11214-008-9467-4.
- McComas, D. J., et al. (2009b), Global observations of the interstellar interaction from the interstellar boundary explorer (IBEX), *Science*, *326*, 959, doi:10.1126/science.1180906.
- Mitchell, D. G., P. C. Brandt, E. C. Roelof, I. Dandouras, M. Krimigis, and B. H. Mauk (2005a), Energetic neutral atom emissions from Titan interaction with Saturn's magnetosphere, *Science*, *308*, 989, doi:10.1126/science.1109805.
- Mitchell, D. G., et al. (2005b), Energetic ion acceleration in Saturn's magnetotail: Substorms at Saturn? *Geophys. Res. Lett.*, *32*, L20S01, doi:10.1029/2005GL022647.
- Mitchell, D. G., et al. (2003), Global imaging of O<sup>+</sup> from IMAGE/HENA, *Space Sci. Rev.*, *109*, 63, doi:10.1023/B:SPAC.0000007513.55076.00.
- Perez, J. D., G. Kozlowski, P. C. Brandt, D. G. Mitchell, J. M. Jahn, and C. J. Pollock (2001), Initial ion equatorial pitch angle distributions from energetic neutral atom images obtained by IMAGE, *Geophys. Res. Lett.*, *28*, 1155.
- Perez, J. D., E. W. Grimes, J. Goldstein, D. J. McComas, P. Valek, and N. Billor (2012), Evolution of CIR storm on 22 July 2009, *J. Geophys. Res.*, *117*, A09221, doi:10.1029/2012JA017572.
- Pollock, C., et al. (2001), First medium enderg energy neutral atom MENA images of Earth's magnetosphere during substorm and storm-time, *Geophys. Res. Lett.*, *28*, 1147.
- Pollock, C. J., A. Isaksson, J.-M. Jahn, F. Søråas, and M. Sørbo (2009), Remote global-scale observations of intense low-altitude ENA emissions during the Halloween geomagnetic storm of 2003, *Geophys. Res. Lett.*, *36*, L19101, doi:10.1029/2009GL038853.1987.
- Roelof, E. C. (1987), Energetic neutral atom image of a storm-time ring current, *Geophys. Res. Lett.*, *14*, 652.
- Roelof, E. C., and A. J. Skinner (2000), Extraction of ion distributions from magnetospheric ENA and EUV images, *Space Sci. Rev.*, *91*, 437.
- Søråas, F., and K. Aarsnes (1996), Observations of ENA in and near a proton arc, *Geophys. Res. Lett.*, *23*, 2959, doi:10.1029/96GL02821.
- Søråas, F., and M. Sørbo (2012), Low altitude observations of ENA from the ring current and from the proton oval, *J. Atmos. Solar-Terr. Phys.*, in press.
- Søråas, F., K. Aarsnes, K. Oksavik, and D. S. Evans (2002), Ring current intensity estimated from low-altitude proton observations, *J. Geophys. Res. Space Physics*, *107*, 1149, doi:10.1029/2001JA000123.
- Valek, P., P. C. Brandt, N. Buzulukova, M.-C. Fok, J. Goldstein, D. J. McComas, J. D. Perez, E. Roelof, and R. Skoug (2010), Evolution of low altitude and ring current ENA emissions from a moderate magnetospheric storm: Continuous and simultaneous TWINS observations, *J. Geophys. Res.*, *115*, A111209, doi:10.1029/2010JA015429.
- Vallat, C., I. Dandouras, P. C. Brandt, and D. G. Mitchell (2004), First comparison between ring current measurements by cluster/CIS and IMAGE/HENA, *J. Geophys. Res.*, *109*, A04213, doi:10.1029/2003JA010224.
- Zoennchen, J. H., U. Nass, G. Lay, and H. J. Fahr (2010), 3D-geocoronal hydrogen density derived from TWINS Ly-alpha data, *Ann. Geophys.*, *28*, 1221, doi:10.5194/angeo-28-1221-2010.